## Exploring layered disorder in lithium-ion conducting Li<sub>3</sub>Y<sub>1-x</sub>In<sub>x</sub>Cl<sub>6</sub>

Ananya Banik,<sup>a\*</sup> Bibek Samanta,<sup>b,c</sup> Bianca Helm,<sup>d</sup> Marvin A. Kraft,<sup>e</sup> Yannik Rudel,<sup>d</sup> Cheng Li,<sup>f</sup> Michael Ryan Hansen,<sup>b</sup> Bettina V. Lotsch,<sup>g</sup> Sebastian Bette,<sup>g\*</sup> and Wolfgang G. Zeier<sup>d,e\*</sup>

<sup>a</sup>Research Institute for Sustainable Energy (RISE), TCG Centre for Research and Education in Science and Technology (TCG-CREST), Kolkata 700091, India.

<sup>b</sup>Institute of Physical Chemistry, University of Münster, Correnstrasse 28/30, 48149 Münster, Germany.

<sup>c</sup>International Graduate School for Battery Chemistry, Characterization,
Analysis, Recycling and Application (BACCARA), Wilhelm-Schickard-Straße 8,
48149 Münster, Germany.

<sup>d</sup>Institute of Inorganic and Analytical Chemistry, University of Münster, Correnstrasse 30, 48149 Münster, Germany.

<sup>e</sup>Institut für Energie- und Klimaforschung (IEK), IEK-12: Helmholtz-Institut Münster, Forschungszentrum Jülich, Corrensstrasse 46, 48149 Münster, Germany.

<sup>f</sup>Neutron Scattering Division, Oak Ridge National Laboratory (ORNL), 1 Bethel Valley Road, Oak Ridge, Tennessee 37831-6473, United States.

<sup>g</sup>Max-Planck-Institute for Solid State Research, Heisenbergstraße 1, 70569

Stuttgart, Germany and Department Chemie, University of Munich (LMU),

Butenandtstraße 5-13 (Haus D), 81377 München, Germany.

\*ananya.banik@tcgcrest.org

\*s.bette@fkf.mpg.de

\*wzeier@uni-muenster.de

**Abstract:** Li<sub>3</sub>Y<sub>1-x</sub>In<sub>x</sub>Cl<sub>6</sub> undergoes a phase transition from trigonal to monoclinic via an intermediate orthorhombic phase. Although the trigonal yttrium containing end member phase, Li<sub>3</sub>YCl<sub>6</sub>, synthesized by a mechanochemical route, is known to exhibit stacking fault disorder, not much is known about the monoclinic phases of the serial composition Li<sub>3</sub>Y<sub>1-x</sub>In<sub>x</sub>Cl<sub>6</sub>. This work aims to shed light on the influence of the indium substitution on the phase evolution, along with the evolution of stacking fault disorder using X-ray and neutron powder diffraction together with solid-state nuclear magnetic resonance spectroscopy studying the lithium-ion diffusion. Although Li<sub>3</sub>Y<sub>1-x</sub>In<sub>x</sub>Cl<sub>6</sub> with  $x \le 0.1$  exhibits an ordered trigonal structure like Li<sub>3</sub>YCl<sub>6</sub>, a large degree of stacking fault disorder is observed in the monoclinic phases for the  $x \ge 0.3$  compositions. The stacking fault disorder materializes as a crystallographic intergrowth of faultless domains with staggered layers stacked in a uniform layer stacking, along with faulted domains with a randomized staggered layer stacking. This work shows how structurally complex even the "simple" series of solid solutions can be in this class of halide-based lithiumion conductors, as apparent from difficulties in finding consistent structural descriptor for the ionic transport.

#### 1. Introduction

Solid-state batteries have historically, but also are more than ever currently discussed as a potential alternative to lithium-ion batteries. Therefore, the search for alternatives to the organic liquid electrolytes led to the discovery of several lithium-ion conducting solid electrolyte families including garnets, <sup>2,3</sup> LISICON-types (lithium superionic conductor)<sup>4</sup> oxides, thio-LISICONs,  $^{5,6}$  Li<sub>10</sub>MP<sub>2</sub>S<sub>12</sub> (M = Si, Ge, Sn),  $^{7,8}$  argyrodite  $^{9-12}$ , ternary lithium halides <sup>13–15</sup> and most recently lithium oxychlorides <sup>16,17</sup>. Although the existence of lithium-ion conducting halides dates back to 1930, <sup>18</sup> Li<sub>3</sub> $MX_6$  (M = Y, Er, In, Sc, Ho, Yb and X = Cl, Br, I)<sup>19–23</sup> regained attention as ambient temperature solid electrolytes in recent years only. This is because the halide solid electrolytes are considered superior compared to oxides, in terms of synthesis, processing as well as their ionic transport. In regards to sulfide-based electrolytes, it is assumed that the oxidative stability is better while exhibiting similar ionic conductivities.<sup>24</sup> However, studies have shown major issues with the use of these materials in terms of chemical stability against sulfide-based solid electrolytes and the lithium metal anode. <sup>25–27</sup> To understand and improve the electrochemical stability and ionic transport in halide-based lithium solid electrolytes, recent studies focused on the thorough structural understanding of these halide materials via cationic and anionic substitution, as well as various synthesis routes.

For instance, isovalent substitution series Li<sub>3</sub>YCl<sub>6-x</sub>Br<sub>x</sub>, <sup>28</sup> Li<sub>3</sub>Y<sub>1-x</sub>In<sub>x</sub>Cl<sub>6</sub>, <sup>29</sup> inducing structural changes which alters the ionic conductivity strongly. Further, aliovalent substitution varies the lithium-ion concentration and therewith, the lithium-ion conductivity in  $Li_{3-x}Y_{1-x}Zr_xCl_{6}$ , <sup>23</sup>  $\text{Li}_{3-x}\text{In}_{1-x}\text{Zr}_x\text{Cl}_6$ , <sup>22</sup> and  $\text{Li}_3M\text{I}_6$  (M=Y; Cd; rare-earth metal, Lu-Sm)<sup>30</sup> is altered. In the case of Li<sub>3</sub>YCl<sub>6</sub>, the introduction of Zr induced a structural transformation from a trigonal to an orthorhombic phase.<sup>23</sup> A similar behavior has been observed for a sodium-ion conductor in which the Na<sub>3-x</sub>Er<sub>1-x</sub>Zr<sub>x</sub>Cl<sub>6</sub> series shows faster ion transport when compared to parent materials, Na<sub>3</sub>ErCl<sub>6</sub> and Na<sub>2</sub>ZrCl<sub>6</sub>.<sup>31</sup> The Li<sub>3-x</sub>In<sub>1-x</sub>Zr<sub>x</sub>Cl<sub>6</sub> compositions depict rather minute change in the ionic conductivity due to change in lithium-ion concentration together with local structural distorsion.<sup>22,32,33</sup> One major advantage of lithium-ion conducting ternary halides is the ease of solution-based synthesis when targeting Li<sub>3</sub>InCl<sub>6</sub>, which suggests easier processing of solid-state batteries.<sup>34,35</sup> However, a strong influence of processing parameters on the structure and ionic conductivity of such halides is generally observed.<sup>20,36</sup> For example, in addition to high-temperature trigonal phase, a metastable trigonal phase with different yttriumion and lithium-ion position was found when the reaction temperature was below 327 °C for  $\text{Li}_3\text{YCl}_6.^{37}$  In another example, the mechanochemically synthesized trigonal phase of  $\text{Li}_2\text{ZrCl}_6$  undergoes a structural transition to a monoclinic phase upon annealing, together with a concurrent decrease in conductivity.<sup>38</sup> Depending on the synthesis conditions, occupational disorder of the central cation, M (M = Y, Er, In, Sc, Ho, Yb and X = Cl, Br, I), was connected to significant changes in the ionic conductivity being suggested in Li<sub>3</sub>YCl<sub>6</sub>,<sup>19,20</sup> and Li<sub>3</sub>YBr<sub>6</sub>.<sup>36</sup> However, the found average positional disorders may just reflect a more complicated underlying mechanism, i.e. stacking faults that were recently found.<sup>39</sup> According to a recent report low temperature synthesis routes may be more prone to the formation of stacking faults,<sup>40</sup> but the direct influence of synthesis route on stacking fault formation is not clear yet.

Lithium-ion conducting ternary halides can be considered as layer-like materials. Here, depending on the cation-anion radius ratio and their polarizability, two different halide frameworks are possible for the ternary lithium halides, i.e. cubic close-packing (ccp) and hexagonal close-packing (hcp), which can lead to the formation of three different structures. <sup>41</sup> The hcp arrangement is the basic building block for the trigonal (Figure 1a) and orthorhombic phases, whereas the monoclinic structure is linked to ccp (Figure 1c). While Li<sub>3</sub>MCl<sub>6</sub> with M = Tb – Tm and Y crystallize in a trigonal polymorph within space group  $P\bar{3}m1$  with Li<sub>3</sub>ErCl<sub>6</sub> structure-type, compounds with M = Yb crystallize in an orthorhombic structure with the Pnma space group. The difference in the two structures is associated with the ordering of the rare-earth metal ions. <sup>41</sup> In the trigonal Li<sub>3</sub>YCl<sub>6</sub>, yttrium-ions can occupy Y(1) (Wyckoff site 1a) in (001) plane and Y(2) (Wyckoff 2d) in (002) plane; yttrium additionally occupies the Y(2') (Wyckoff 2d) in (001) plane (Figure 1a). Trigonal Li<sub>3</sub>YCl<sub>6</sub> has two different lithium-ion sites, Li(1) (Wyckoff positions 6g) and Li(2) (Wyckoff 6h); Edge sharing LiCl<sub>6</sub><sup>5-</sup> units forms a honeycomb-type of arrangement in both the (001) and (002) planes (Figure 1b).

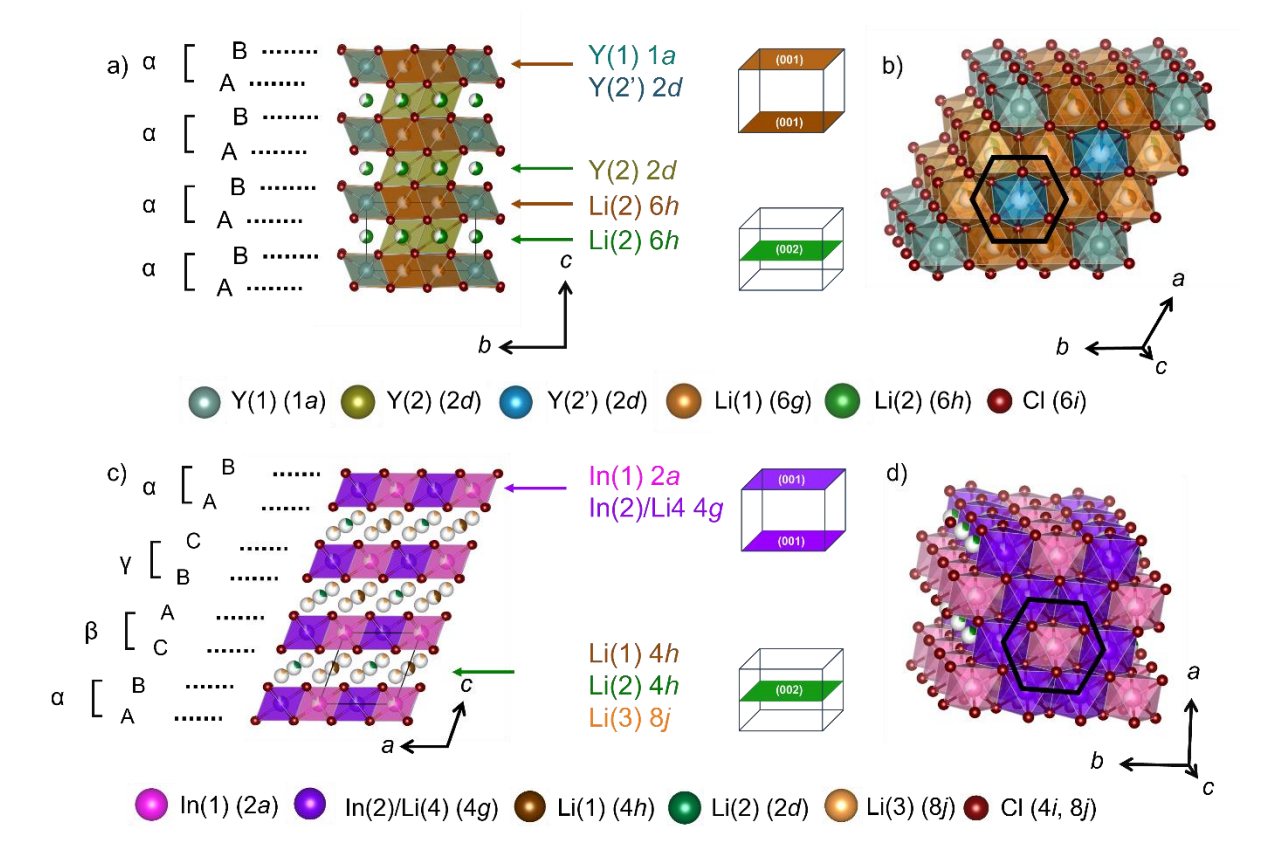


**Figure 1.** a) Hexagonal and c) cubic close-packing of chlorides in the trigonal Li<sub>3</sub>YCl<sub>6</sub> and monoclinic Li<sub>3</sub>InCl<sub>6</sub> phase, respectively. The layer stacking sequences are represented by small Greek letters and the stacking order of the anion substructure is represented by capital Latin letters. Randomly occurring changes in stacking sequence of the cation layers generate stacking faults in the layered Li<sub>3</sub>Y<sub>1-x</sub>In<sub>x</sub>Cl<sub>6</sub> structure, whereas the anion substructure remains cubic close-packed. For better understanding, (001) and (002) planes are marked in the schematic unit cells. b) and d) show the octahedral halide framework in trigonal and monoclinic phases, respectively, in which the central metal and lithium-ions occupy some of the octahedral voids forming the honeycomb network, marked in black. Based on the position of the occupied octahedral void, the hexagonal close-packing can result in the trigonal or orthorhombic structure. The occupation of the octahedral voids in the cubic closed-packed structure generates the monoclinic crystal structure.

In contrast, Li<sub>3</sub>InCl<sub>6</sub>, Li<sub>3</sub>ScCl<sub>6</sub>, and Li<sub>3</sub>MBr<sub>6</sub> with M = Sm - Lu adopt a *ccp*-type of the halide anion framework and a monoclinic structure with C2/m space group.<sup>41,42</sup> In the case of Li<sub>3</sub>InCl<sub>6</sub>, indium is known to occupy In(1) (Wyckoff 2*a*) and In(2)/Li(4) (Wyckoff 4*g*) sites in (001) plane. Recent work on monoclinic Li<sub>3</sub>HoBr<sub>6-x</sub>I<sub>x</sub> substitution series shows that cation-site

disorder in (001) plane strongly influences the lithium-ion dynamics. 40 Lithium-ions occupy Li(1) (Wyckoff 4h), Li(2) (Wyckoff 2d), Li(3) (Wyckoff 8j) in (002) plane along with the disordered In(2)/Li(4) (Wyckoff 4g) sites. Although Li<sub>3</sub>MCl<sub>6</sub> can crystallize in a trigonal, orthorhombic, or monoclinic structure, their structures are analogous to the O3-type LiCoO2 structure. 43,44 In LiCoO<sub>2</sub>, the transition metal slab consists of edge sharing (CoO<sub>6</sub>)<sup>3-</sup> octahedra and the lithium-ion are sandwiched between the (CoO<sub>6</sub>)<sup>3-</sup> slabs. The general formula of the ternary halides, Li<sub>3</sub>MCl<sub>6</sub>, can be rewritten as Li<sub>1/3</sub>(Li<sub>2/3</sub>M<sub>1/3</sub>)Cl<sub>2</sub>, in which the (CoO<sub>6</sub>)<sup>3-</sup> slab is replaced by partially occupied and edge sharing the MCl<sub>6</sub> and LiCl<sub>6</sub> slabs. Partially occupied lithium-ion in the (002) plane forms edge sharing (LiCl<sub>6</sub>)<sup>5-</sup> octahedra, in which chloride-ions are already accounted for in the  $(MCl_{6/3})^{3-}$ , and  $(LiCl_{6/3})_{5-}$  polyhedra from the (001) plane (Figure 1c). As a result, the structure exhibits a honeycomb layer of edge sharing (Li/M)Cl<sub>6</sub> octahedra, in which the interstices are partially occupied by central metal (M) ions (Figure 1b, d). Because of the layer-like geometry with honeycomb arrangement, these compounds are prone to exhibit stacking fault disorder. 45–47 Recent reports confirm the presence of stacking fault in various ternary halides including Li<sub>3</sub>YCl<sub>6</sub>,<sup>39</sup> Li<sub>3</sub>YCl<sub>3</sub>Br<sub>3</sub>,<sup>28</sup> Li<sub>3</sub>HoBr<sub>6-x</sub>I<sub>x</sub><sup>40</sup> and Li<sub>3</sub>MI<sub>6</sub><sup>30</sup>, where M = rare-earth metal. An example of ideal stacking sequence and the faulted sequence is shown for the Li<sub>3</sub>InCl<sub>6</sub> structure in Figure 2. The ideal stacking sequence of layers can be described by a stacking vector S1, shown in Figure 2a, which is identical with the c-axis of monoclinic Li<sub>3</sub>InCl<sub>6</sub> lattice. Based on the relative cation position of the next layer, forming honeycomb framework, three different stacking vectors are possible. An exemplary different stacking sequence with stacking vector S2 is shown in Figure 2b, where the Cl sublattice follows an ABCABC stacking, but the cation, M(2)/Li occupies a  $\beta 2$  position instead of  $\beta 1$ . However, a combination of the site disorder of central cation, M and stacking fault makes the structural analysis complicated. Often, stacking disorder is misinterpreted as cation-site disorder. A method to deconvolute site disorder and faulting was developed for  $Li_3HoBr_{6-x}I_x$ , which shows a less dominant influence of stacking disorder on the lithium-ion dynamics over site disorder. <sup>40</sup> As previous works show the structural complexity of these compounds, <sup>39,40</sup> here we study a series of layered-type ternary halides to understand the influence of substitution on the structure, stacking fault, cation disorder and resulting ionic transport properties.

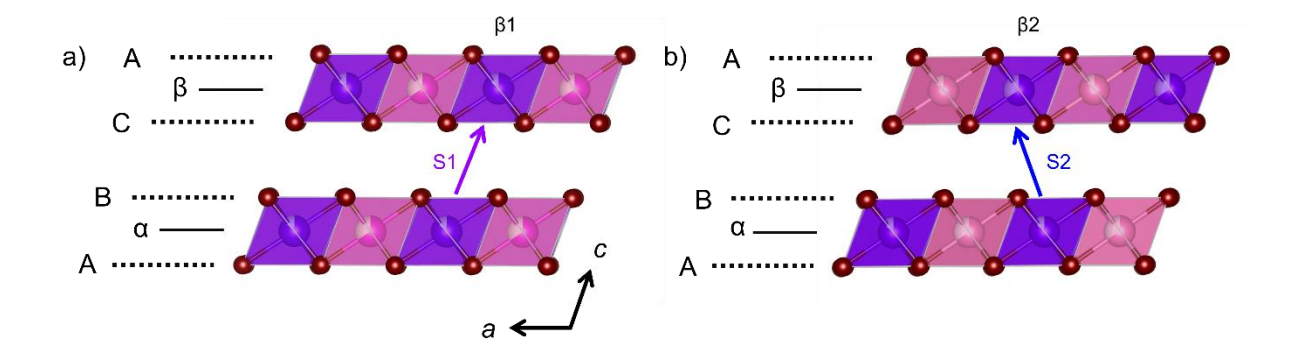


**Figure 2.** Possible layer stacking patterns in the monoclinic Li<sub>3</sub>InCl<sub>6</sub> phase where the lithiumion layer has been omitted for clarity. Three types of stacking sequences are possible based on the relative position of atoms forming a honeycomb arrangement in different layers. a) Stacking pattern of ideal faultless monoclinic phase is represented with stacking vector S1. Here,  $\alpha$  and  $\beta$  denotes the layer stacking sequence. b) An exemplary alternate stacking sequence is shown in which the stacking vector is S2. β1 and β2 correspond to the relative cationic position in the lattice, which form honeycomb pattern.

In this work, we study the influence of indium substitution on the phase evolution and ionic transport of Li<sub>3</sub>Y<sub>1-x</sub>In<sub>x</sub>Cl<sub>6</sub> having a layer-type structure with honeycomb (LiCl<sub>6</sub>)<sup>5-</sup> polyhedral arrangements. Using X-ray diffraction, high-resolution neutron diffraction, impedance spectroscopy, and solid-state nuclear magnetic resonance spectroscopy, we aim to understand the evolution of stacking faults and the lithium-ion substructure. This work shows that a "simple" series of solid solutions in these halide compounds exerts itself in crystallographic intergrowths of faulted and faultless domains, showing that structure – transport correlations may not always be straightforward in halide-based lithium-ion conductors.

## 2. Experimental section

**Synthesis.** All synthesis steps were performed under Ar-atmosphere. To prepare  $\text{Li}_3\text{Y}_{1-x}\text{In}_x\text{Cl}_6$ . a classic high-temperature solid-state synthesis was adopted using LiCl (ChemPur, 99.99 %), YCl<sub>3</sub> (Alfa Aesar, 99.999%) and InCl<sub>3</sub> (99.999%, trace metal basis, Sigma Aldrich) as reaction precursors. Stoichiometric amounts of precursors for obtaining 1 g product were mixed and hand ground in an agate mortar, followed by pellet preparation and then filled into a pre-dried (800 °C) quartz ampule, which was subsequently sealed under vacuum. Only for Li<sub>3</sub>YCl<sub>6</sub> synthesis, 10 wt.% excess YCl<sub>3</sub> was used, as mentioned elsewhere, 20 which allow us to compare the reported structural information of Li<sub>3</sub>YCl<sub>6</sub> with Li<sub>3</sub>Y<sub>0.9</sub>In<sub>0.1</sub>Cl<sub>6</sub> and help to understand the influence of indium substitution on the Li<sub>3</sub>YCl<sub>6</sub> structure. Ampules were heated to desired temperature with heating rate of 100 °C·h<sup>-1</sup>. Since Li<sub>3</sub>InCl<sub>6</sub> has an incongruent melting point of 444 °C, 42 the synthesis temperature had to be lowered with increasing indium content. The reactions were performed at 550 °C (Li<sub>3</sub>YCl<sub>6</sub>), 450 °C (Li<sub>3</sub>Y<sub>1-x</sub>In<sub>x</sub>Cl<sub>6</sub>,  $0.1 \le x \le$ 0.7), 400 °C (Li<sub>3</sub>Y<sub>0.2</sub>In<sub>0.8</sub>Cl<sub>6</sub>) and 280 °C (Li<sub>3</sub>Y<sub>1-x</sub>In<sub>x</sub>Cl<sub>6</sub>,  $0.9 \le x \le 1$ ). For completion of reaction, the annealing duration was always set to one week followed by natural cooling step. For all the analysis discussed in below, we have considered nominal stoichiometry of elements from the compositions.

*X-ray powder diffraction.* The diffraction patterns (Figure 3) of the Li<sub>3</sub>Y<sub>1-x</sub>In<sub>x</sub>Cl<sub>6</sub> phases were collected on laboratory powder X-ray diffractometers in Debye-Scherrer geometry (Stadi P-Diffractometer (Stoe), Ag-K<sub> $\alpha$ 1</sub> or Mo-K<sub> $\alpha$ 1</sub> radiation from primary Ge(111)-Johann-type monochromator, triple array of Mythen 1 K detectors (Dectris). The samples were sealed in 0.3 mm diameter borosilicate glass capillaries (Hilgenberg glass), which were spun during the measurement. The data were collected in a  $2\theta$  range between 0 and  $110^{\circ}$  applying a total scan duration of three hours.

*Neutron powder diffraction.* Neutron powder diffraction data of all compositions  $\text{Li}_3\text{Y}_{1-x}\text{In}_x\text{Cl}_6$   $(0.1 \le x \le 1)$  were collected at Oak Ridge spallation neutron source (SNS, Oak Ridge National Laboratory) using the PAC automatic sample changer at POWGEN diffractometer (BL-11A beamline). Under inert conditions, the samples (~1.2 g) were loaded into a cylindrical vanadium can (inner diameter – 6 mm) which was sealed with a copper gasket to avoid exposure to air during the measurement. The diffractograms were collected for four hours in high-resolution mode using a single bank with a center wavelength of 1.5 Å. Absorption corrected data (Figure S1) were used to analyze the structure.

Diffraction based 2D defect analyses. Rietveld refinement was employed on the X-ray powder diffraction data of Li<sub>3</sub>Y<sub>1-x</sub>In<sub>x</sub>Cl<sub>6</sub>. The program TOPAS 6.0 was used to analyze the X-ray powder diffraction patterns.<sup>48</sup> The background of the diffraction patterns was modelled by Chebychev polynomials of 6<sup>th</sup> order and the peak profile by using the fundamental parameter approach implemented into TOPAS.<sup>49,50</sup> The instrumental resolution function had been determined by a Pawley fit<sup>51</sup> of a LaB<sub>6</sub> standard measurement prior to the experiments. Changes in lattice parameters are shown in Figure 4.

*Trigonal phase*. Trigonal Li<sub>3</sub>Y<sub>1-x</sub>In<sub>x</sub>Cl<sub>6</sub> with x = 0 and 0.1 could be modeled using Rietveld refinement, shown in Figure S2 and S3a, respectively; structural information reported by Schlem *et al.* was used as the starting model.<sup>20</sup>

Monoclinic phase. A two-phase model including an ordered monoclinic structure where In/Y occupy In(1), lithium-ions occupy Li(1) and Li(2) sites and a stacking faulted monoclinic phase were used to refine the diffraction data of Li<sub>3</sub>Y<sub>1-x</sub>In<sub>x</sub>Cl<sub>6</sub> with  $0.2 \le x \le 1.0$  to quantify the stacking fault disorder, since it was not possible to fit the diffraction data using only single phase monoclinic model. Representative refinement plot is given in Figure S4, for Li<sub>3</sub>Y<sub>0.5</sub>In<sub>0.5</sub>Cl<sub>6</sub> showing the limits of Rietveld refinement in terms of analyzing the faulted phases, which can be overcome by using the stacking fault model (Figure 5a).

For the stacking faulted phase, the layer constitution was derived from the structure dataset given by Schmidt *et al.* and like for the ordered phase In/Y was put on the 2*a* site, exclusively.<sup>52</sup> For the refinement, a recursive supercell approach implemented into TOPAS<sup>53,54</sup> was used that calculates X-ray patterns from randomly created stacks of layers and averages them. Therefore, the monoclinic unit cell was transformed into a pseudo-orthorhombic cell with space group *P*1 according to a procedure described elsewhere.<sup>46,47</sup> From the layer constitution, we derived possible stacking vectors and a faulting scenario in which the staggered stacking of the layers becomes randomized as described in previous works.<sup>46,47</sup> For each refinement, the diffraction patterns of 100 stacks consisting of 200 layers were averaged. For the final Rietveld refinement, constraints were applied on the atomic positions to maintain the intra-layer symmetry.<sup>47</sup> Further details of the models used for the refinement are given in the results section and Supporting information (Figure S5 and S6). For getting an idea in the estimated standard deviation (ESD), we performed selected refinements up to 10 times and tracked the results of the pseudo-quantitative analyses. We noticed fluctuations in the content of ordered and disordered Li<sub>3</sub>Y<sub>1</sub>-

 $_x$ In $_x$ Cl $_6$  phase of up to 0.6 wt-%. Considering the fact that there is some parameter-correlation, we multiplied this ESD times 3, yielding 1.8 wt-% and rounded to 2.0 wt-%.

## Rietveld analysis of neutron diffraction data.

*Trigonal structure.* As the X-ray diffraction data of Li<sub>3</sub>Y<sub>0.9</sub>In<sub>0.1</sub>Cl<sub>6</sub> and Li<sub>3</sub>YCl<sub>6</sub> do not show any indication of stacking fault disorder, we refined the absorption corrected neutron diffraction data of Li<sub>3</sub>Y<sub>0.9</sub>In<sub>0.1</sub>Cl<sub>6</sub> samples with TOPAS Academics 6.0 software package (Figure S3b)<sup>48</sup> and compared with previously reported Li<sub>3</sub>YCl<sub>6</sub> data<sup>36</sup> to understand the influence of indium substitution on the structure of trigonal Li<sub>3</sub>Y<sub>1-x</sub>In<sub>x</sub>Cl<sub>6</sub> phase. The profile refinement includes 1) the background and scaling factors for the main and side phase, 2) lattice parameters, and 3) peak-shape function, which was convolution of a pseudo-Voigt and GSAS back-to-back exponential function to obtain a good profile fit.<sup>55</sup> The crystallographic information file of previously reported trigonal Li<sub>3</sub>YCl<sub>6</sub> (for x = 0.1)<sup>20</sup> is used without 2*d* site for metal cation on the (001) plane as the starting model based on the result obtained from refinement of the X-ray diffractogram.

For the structural refinement, 4) displacement parameters, occupancies and positions were refined for central metal cation (indium and yttrium) followed by halide anions. Displacement parameters from all the central metal-ion sites were constrained to improve the fit stability. To reduce the number of free variables, the indium occupancy was constrained to the nominal yttrium and indium content (Table S1). After refinement of the immobile framework, 5) the lithium-ion displacement parameters, occupancies and site coordinates were refined; parameters from all other atoms were kept constant. Like yttrium and indium, the lithium-ion content was constrained to the nominal stoichiometry. 6) All the non-lithium octahedral and tetrahedral positions were evaluated for possible lithium-ion occupancy. The central metal occupies Y(1) and Y(2) positions on the (002) lattice plane. We found lithium-ion on Li(1) and Li(2) sites as shown in a previous report.<sup>20</sup> All possible octahedral interstitial sites both for yttrium-ion and lithium-ion were tested; No additional occupied sites were found.

7) Next, thermal displacement parameters, occupancies, and coordinates of all the sites were refined together. At the very end, lithium-ion occupancy on the Y(2') position was checked. Lithium-ion occupies this position partially. All the structural information obtained from the refinement is compiled in Figure 6a and Table S2.

*Monoclinic structure*. The two-phase model obtained from X-ray powder diffraction data refinement (Figure S5 and S6) was used to model the neutron diffraction data (Figure S7-S9).

Only the lithium-ion occupancies were allowed to refine constraining all the other parameters to the X-ray diffraction results. Lithium-ion substructures from our previous report<sup>22</sup> is used for the neutron data refinement. A detailed discussion of the refinements can be found in the result section (Figure 6b). Refinement constraints are given in Table S3. Representative refinement parameters are given in Table S4 for Li<sub>3</sub>Y<sub>0.5</sub>In<sub>0.5</sub>Cl<sub>6</sub>.

 $R_{wp}$  and GoF values for all the diffraction data of Li<sub>3</sub>Y<sub>1-x</sub>In<sub>x</sub>Cl<sub>6</sub> are in Table S5. The GoF appears high for the neutron data refinement. This is however, attributed because the software used for the refinements (TOPAS 6.0) calculated the GoF by division of  $R_{wp}$  by  $R_{exp}$ .  $R_{exp}$  is internally estimated by the counting statistics and usually significantly underestimated for data measured with noise-free detectors, i.e. synchrotron data or neutron data.

## Nuclear Magnetic Resonance (NMR) Spectroscopy.

 $^6$ Li magic-angle spinning (MAS) NMR measurement. Solid-state  $^6$ Li MAS NMR experiments were performed on a Bruker DSX 500 spectrometer equipped with a 11.74 T wide-bore magnet using a 4 mm Bruker MAS probe at a Larmor frequency of  $\omega_0/2\pi = 73.6$  MHz. As our aim was to study the influence of indium on the lithium-ion coordination environment to understand the presence of stacking fault,  $^6$ Li MAS NMR experiments were done on Li<sub>3</sub>Y<sub>1-x</sub>In<sub>x</sub>Cl<sub>6</sub> with  $x \ge 0.1$  (Figure 7a). Radiofrequency pulses of 3.0-6.0 μs at 120 W power as  $\pi/2$ -pulse and a relaxation delay of 15 s were used for the single-pulse MAS NMR experiments executed at a spinning frequency of 12.5 kHz. Magic-angle calibration was performed using the  $^{23}$ Na spinning sideband pattern from solid NaNO<sub>3</sub> under MAS conditions. The  $^6$ Li chemical shift was referenced to  $^6$ Li-enriched solid Li<sub>2</sub>CO<sub>3</sub> at 0.00 ppm. Powdered samples were packed into cylindrical-type 4 mm zirconia rotors under Ar-atmosphere of glovebox (H<sub>2</sub>O < 0.5 ppm, O<sub>2</sub> < 0.5 ppm). Spectral analysis based on the lithium-ion content obtained from refinement of neutron powder diffraction data are shown in Figure S10.

<sup>7</sup>Li NMR  $T_1$ -relaxation measurement. Static variable temperature saturation recovery <sup>7</sup>Li NMR experiments were recorded on a Bruker Avance III 300 spectrometer connected to a wide-bore magnet of 7.05 T nominal magnetic field for Li<sub>3</sub>Y<sub>1-x</sub>In<sub>x</sub>Cl<sub>6</sub> for  $x \ge 0.3$  (Figure 7b, S11 and S12). This magnetic field corresponds to a Larmor frequency of  $\omega_0/2\pi = 79.39$  MHz for <sup>7</sup>Li. A radio-frequency pulse of 2.5 μs length at 120 W was used as  $\pi/2$ -pulse. Recovery delay lengths were varied from  $t_1 = 10$  μs to  $t_{31} = 316.23$  s with four steps increment per decade. The FIDs (free-induction decays) were Fourier-transformed to obtain frequency-domain signals which were integrated in the TopSpin software and corresponding signal intensity curves were fitted with

exponential type of saturation function with a stretching exponent. The data were recorded in the temperature range from 220-420 K and a 20 min of waiting period for temperature stabilization was used at each measurement temperature.  $N_2$  gas flow and electrical heating was utilized to regulate the temperature. In the sub-room temperature (T < 300 K) range, cooled  $N_2$  gas flow from an Air Jet XR compressor from SP Scientific (FTS Systems) regulated the temperature whereas an uncooled stream of  $N_2$  gas was utilized for temperature stabilization in T > 300 K range. Temperature calibration was done using temperature-dependent  $^1$ H NMR signal-shifting of methanol (220-290 K) and ethylene glycol (320-420 K) $^{56}$ .

For x = 0.1 and 0.2,  $T_1$ -relaxation measurements were not performed as lithium-ion dynamics in the MHz regime cannot be probed for these samples due to their poor ionic conductivity (as observed in EIS measurement in Figure S14). In general, no rate-maxima is expected for such poor conducting materials within our achievable experimental temperature range, prohibiting any qualitative comparison of dynamic processes to those observed in relatively faster ionic conductors in the series i.e.  $x \ge 0.3$ .

Electrochemical impedance spectroscopy. Ionic conductivities were measured by potentiostatic electrochemical impedance spectroscopy (PEIS) for Li<sub>3</sub>Y<sub>1-x</sub>In<sub>x</sub>Cl<sub>6</sub> with  $x \ge 0.1$ using a homebuilt cell casing where stainless steel current collectors are used. Since our main focus in this work was to understand the influence of indium content on the phase evolution and associated change in lithium-ion diffusion of Li<sub>3</sub>Y<sub>1-x</sub>In<sub>x</sub>Cl<sub>6</sub> series, we have not measured PEIS for the unfaulted trigonal Li<sub>3</sub>YCl<sub>6</sub>. Instead, we used the transport properties of Li<sub>3</sub>YCl<sub>6</sub>, previously reported by Schlem et al., synthesized by classic solid-state synthesis for comparison.<sup>20</sup> For a typical measurement, approximately 200 mg of each sample were filled into a 10 mm inner diameter cylindrical PEEK (polyether ether ketone) inlet of the cell case and subsequently pressed uniaxially with 374 MPa for three minutes followed by a slow pressure release. Next, stainless steel current collectors, which also work as the blocking electrodes for the impedance measurements, are connected to the SE pellet using a constant pressure of 10 Nm on the cell screws. Details of cell setup can be found elsewhere.<sup>57</sup> All obtained geometrical pellet densities were around 80-90% of the crystallographic density. The impedance measurements were performed with a SP300 impedance analyzer (Biologic) in a temperature range of 233 K to 313 K and applying a sinusoidal excitation voltage within a frequency range of 7 MHz to 100 mHz and applying an amplitude of 10 mV. The spectra analyses were carried out with the RelaxIS 3 software (rhd instruments) (Figure S14 and S15). Reported conductivities are from the impedance measurements collected in the direction

parallel to the pellet pressing direction. The uncertainty of conductivity and activation energy  $(1\sigma)$  were estimated from the fit errors and geometrical uncertainties of the pellets.

## 3. Results

#### Phase evolution in Li<sub>3</sub>Y<sub>1-x</sub>In<sub>x</sub>Cl<sub>6</sub>

To shed light on the influence of substituting Y with In, the  $Li_3Y_{1-x}In_xCl_6$  substitution series was synthesized in steps of x = 0.1 using a high-temperature solid-state synthesis route. The reaction temperature was varied from 550 °C to 280 °C based on the thermal stability of the product.<sup>42</sup> X-ray powder diffraction analyses (Figure 3a) show that the solid-state synthesis yields almost pure samples of the Li<sub>3</sub>Y<sub>1-x</sub>In<sub>x</sub>Cl<sub>6</sub> solid solution series. LiCl was found as a minor impurity (3-5 wt.%) in all synthesized samples except for Li<sub>3</sub>YCl<sub>6</sub>. Compositions of the solid solution series with a very high yttrium content, x = 0 and x = 0.1, crystallize in the trigonal  $\text{Li}_3\text{YCl}_6$  structure type in space group  $P\overline{3}m1$ . According to X-ray powder diffraction data refinement, for both compounds fully weighted Rietveld refinements showed that the Y(2') position (Y at 2d position at 1/3, 2/3, 0) is vacant, which is to be expected for materials obtained by high-temperature solid-state synthesis because of strong electrostatic repulsion with the adjacent yttrium site. Refinements against neutron powder diffraction data of Li<sub>3</sub>Y<sub>1-x</sub>In<sub>x</sub>Cl<sub>6</sub> with x = 0.1 show similar yttrium site occupancy. Aiming for 20 at.-% indium substitution of yttrium (x = 0.2) yields a multiphase mixture with orthorhombic (space group Pnma)<sup>41</sup> (56 wt.%), monoclinic (27 wt.%) and trigonal (13 wt.%) phase of varying compositions of Li<sub>3</sub>Y<sub>1-x</sub>In<sub>x</sub>Cl<sub>6</sub> along with minor LiCl impurities (4 wt.%) (Figure S16a). A further increase in the indium content leads to the formation of the monoclinic structure type. With the indium content > 30 at.-%, the reflections gradually shift towards higher Q (Figure S16b), indicating substitution of yttrium by indium, which is associated with a contraction of the unit cell. Considering the smaller ionic radius of  $In^{3+}$  (VI, r = 0.8 Å) compared to  $Y^{3+}$  (VI,  $r = 0.9 \text{ Å})^{58}$ , this trend can be expected. Between x = 0.3 and x = 1.0 the behavior is almost linear and follows Vegard's law (Figure 4). Upon transition from the trigonal to the monoclinic structure type, the unit cell volume increases (Figure 4d), which is mainly caused by a rise in the b-lattice parameter and the interlayer distance, i.e. d(001) (Figure 4b, c). This can be explained by the distortion of the layer materializing in a decrease of the lattice symmetry from trigonal to monoclinic and by the relocation of half of the rare earth metal cations from the interlayer positions in the trigonal form to the intra-layer voids in the monoclinic form, where the interlayer cation positions are occupied by lithium-ions, exclusively.

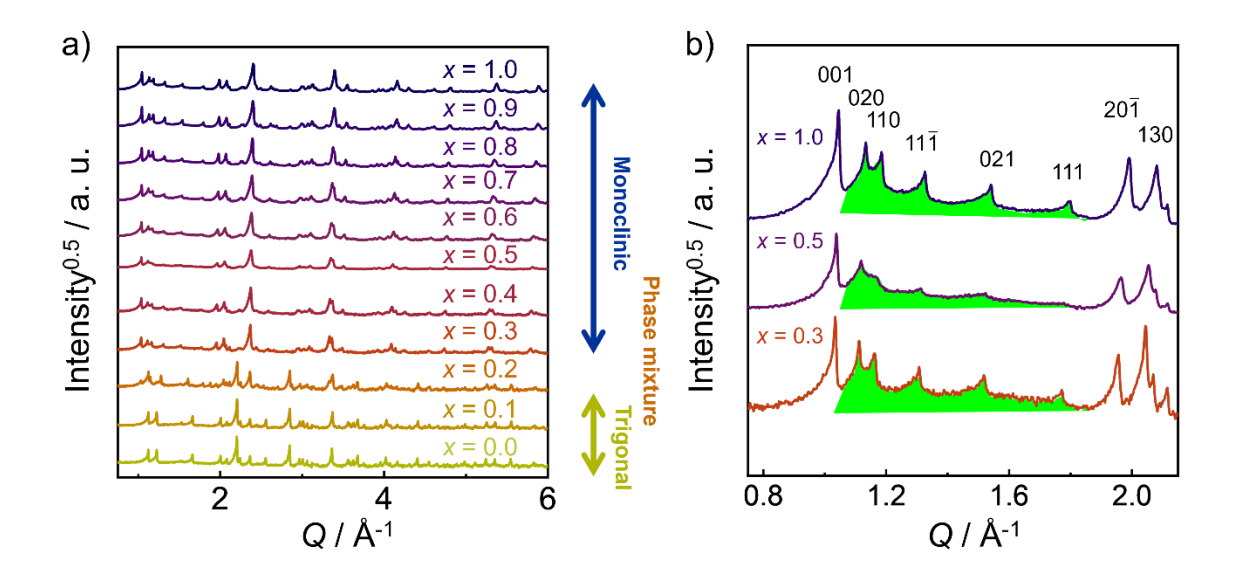


**Figure 3.** a) Room temperature X-ray powder diffraction data for Li<sub>3</sub>Y<sub>1-x</sub>In<sub>x</sub>Cl<sub>6</sub> for x = 0.0 - 1.0 including the assignment to the different Li<sub>3</sub>MCl<sub>6</sub> structure types. b) Characteristic triangular peak shapes (marked in green) indicating planar disorder are highlighted.

Another striking feature in the diffraction patterns of the monoclinic range of Li<sub>3</sub>Y<sub>1-x</sub>In<sub>x</sub>Cl<sub>6</sub> is the presence of diffuse scattering between the (020) and (111) reflections (Figure 3b). The characteristic triangular peak shape indicates stacking fault disorder, <sup>59,60</sup> as frequently observed in layered compounds with honeycomb motifs. 61,62 This effect is most pronounced for the sample x = 0.5, shown in Figure S17 but also clearly visible for all samples. Due to the faulting, it is not possible to refine the structure using standard Rietveld refinements of only the ordered monoclinic phase (see Figure S4). The diffraction patterns are comparable to their stacking faulted structural analogues Li<sub>3</sub>MBr<sub>6-x</sub>I<sub>x</sub>;<sup>30,40</sup> hence the same structural model is used to quantify the stacking fault disorder. The optimization of the fault probabilities using grid search routines, 46,47 however, led to insufficient fits of the diffraction data. If the fault probability is incrementally increased, reflections like (020), (110),  $(11\overline{1})$ , (021) and (111) are broadened and a broad, triangular-shaped peak appears underneath these peaks, as seen in Figure 3b. 46 In the the triangular-shaped measured data. however, we find both diffuse scattering and comparatively sharp Bragg reflections.

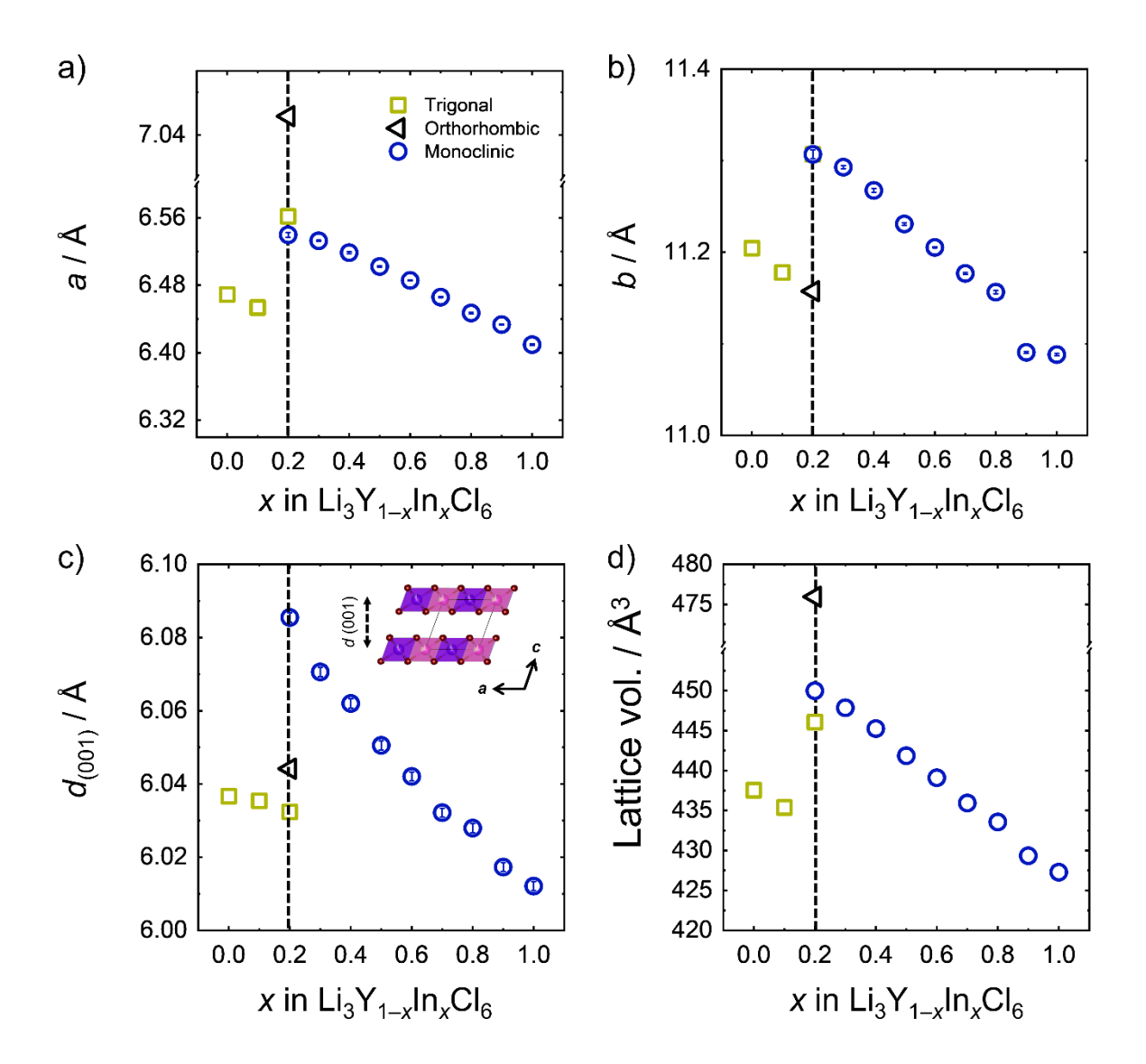


**Figure 4.** a-d) Change in lattice parameters with indium substitution in  $\text{Li}_3\text{Y}_{1-x}\text{In}_x\text{Cl}_6$  from the X-ray diffraction data refinement. Lattice parameters of trigonal and orthorhombic phases are transformed to those of the monoclinic equivalent to understand the influence of indium substitution on the lattice parameters. The dashed line represents the transition from the trigonal structure type to the monoclinic type via the mixed phase formation consisting of trigonal, orthorhombic, and monoclinic structures at x = 0.2.

Consequently, a low fault probability leads to proper modelling of the Bragg reflections but to an insufficient description of the diffuse scattering and applying a high fault probability leads to the opposite effect. The measured diffraction data indicate intergrown domains of randomly oriented honeycomb layers and faultless stacked honeycomb layers. An intergrowth of layers having different stacking orders has already been observed for NiCl(OH)<sup>63</sup> and SnTiO<sub>3</sub><sup>64</sup>, with the latter one also showing honeycomb motifs. Similarly, the diffraction data of Li<sub>3</sub>IrO<sub>3</sub>(OH)<sub>3</sub>,

which is structurally closely related to monoclinic Li<sub>3</sub>Y<sub>1-x</sub>In<sub>x</sub>Cl<sub>6</sub>, indicated the presence of small, ordered domains within a randomly oriented stacking of staggered honeycomb layers.<sup>46</sup> Accordingly, we used a two-phase model for the refinement of the diffraction data. For the disordered "monoclinic phase with stacking faults" the fault probability was maximized, meaning the staggered stacking of the honeycomb layer fully randomized. For the ordered monoclinic phase, the fault probability was set to zero. Both phases were constrained as described elsewhere. <sup>64</sup> Refined data are shown in Figure 5a and S4-S6. An increasing indium content leads to a larger phase fraction of the stacking faulted monoclinic phase (Figure 5b) up to the composition with 50 at.-% indium is reached. For the indium richer members of the solid solution series, the phase fraction of stacking faulted Li<sub>3</sub>Y<sub>1-x</sub>In<sub>x</sub>Cl<sub>6</sub> is decreasing again. In general, the amount of stacking faulted Li<sub>3</sub>Y<sub>1-x</sub>In<sub>x</sub>Cl<sub>6</sub> clearly exceeds the amount of ordered phase for all members of the solid solution series (Figure S18), which is another example of the notoriously stacking faulted character of layered honeycomb-type compounds. A recent report from Sebti et al. shows stacking fault in Li<sub>3</sub>YCl<sub>6</sub> can be altered by changing the synthesis route. Li<sub>3</sub>YCl<sub>6</sub> prepared via ball milling show stacking fault where as high-temperature solidstate route leads to ordered trigonal phase.<sup>39</sup> A strong influence of synthesis temperature on stacking fault is observed for Li<sub>3</sub>HoBr<sub>6-x</sub>I<sub>x</sub>. <sup>40</sup> Low temperature synthesis (below 300 °C) results in higher degree of stacking fault for Li<sub>3</sub>HoBr<sub>6</sub> and lower iodine containing samples from Li<sub>3</sub>HoBr<sub>6-x</sub>I<sub>x</sub> series; a rise in synthesis temperature leads to reduced concentration of stacking fault. However, while a phase transformation and average long range ionic transport of Li<sub>3</sub>Y<sub>1-x</sub>In<sub>x</sub>Cl<sub>6</sub> is reported, changes in the lithium-ion substructure associated with the trigonal to monoclinic phase transformation has not been investigated. Additionally, it is important to understand the effect of stacking faults on the lithium ionic substructure of the monoclinic phase, which may further explain the ionic transport trend in these materials.

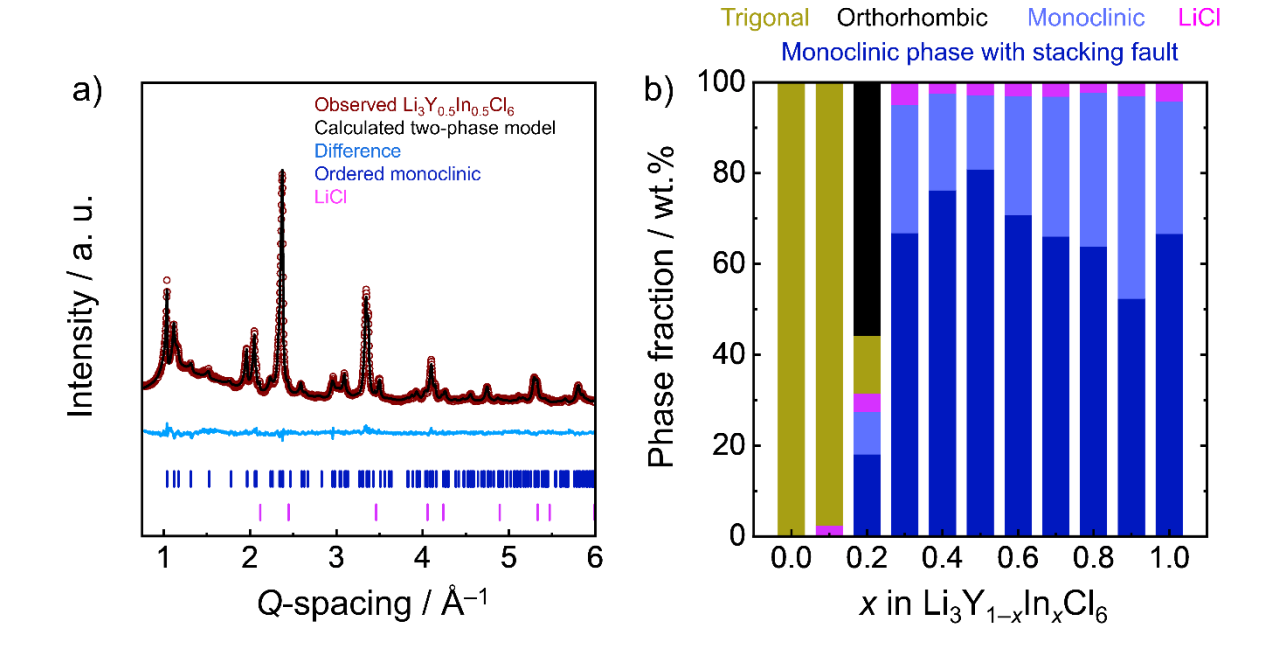


**Figure 5.** a) Refinement of the X-ray diffraction data of Li<sub>3</sub>Y<sub>0.5</sub>In<sub>0.5</sub>Cl<sub>6</sub> with a two-phase approach including an ordered and stacking faulted structure model. b) Distribution of phase fraction as function of x in Li<sub>3</sub>Y<sub>1-x</sub>In<sub>x</sub>Cl<sub>6</sub>. A small weight fraction (3-4 wt. %) of LiCl was observed for  $x \ge 0.1$ . The monoclinic phases consist of a combination of the ordered structure as well as faulted structure. Uncertainty in phase fraction determination is expected to be in the range of  $\pm 2$  wt.%.

### Lithium substructure

*Trigonal polymorph*. To analyze the influence of indium substitution on the lithium-ion substructure of  $\text{Li}_3Y_{1-x}\text{In}_x\text{Cl}_6$ , the neutron diffraction data (Figure S1) of this substitution series is analyzed. Figure 6 summarizes the lithium-ion substructure of  $\text{Li}_3Y_{1-x}\text{In}_x\text{Cl}_6$ . As the trigonal  $\text{Li}_3Y_{0.9}\text{In}_{0.1}\text{Cl}_6$  does not show any indication of stacking fault in X-ray powder diffraction, the refinement on the neutron diffraction is performed considering a single-phase material in its trigonal phase (Figure S3b). Lithium-ions occupy the Li(1) and Li(2) positions in the trigonal  $\text{Li}_3Y\text{Cl}_6$ . The lithium polyhedral volume does not change significantly upon indium substitution for the trigonal phase, whereas the occupancy on Li(1) and Li(2) positions decrease slightly (Figure 6a). In addition to the usual lithium-ion positions, lithium-ion occupancy was found on the Y(2') position in the (001) plane, indicating facile lithium-ion diffusion within the (001) plane for Li<sub>3</sub>Y<sub>0.9</sub>In<sub>0.1</sub>Cl<sub>6</sub>. Unfortunately, the neutron diffraction data of x = 0.2 cannot

be analyzed for the lithium-ion substructure, as it is a complex phase mixture of trigonal, orthorhombic, and monoclinic phases.

*Monoclinic polymorph.* From x = 0.3 onwards, Li<sub>3</sub>Y<sub>1-x</sub>In<sub>x</sub>Cl<sub>6</sub> exerts itself as a monoclinic phase mixture that is comprised of a monoclinic phase with stacking faults along with an ordered monoclinic phase. Stacking fault disorder is harder to track in the neutron diffraction data as the diffraction pattern is mainly governed by the chloride substructure (coherent scattering cross section of Cl  $\approx 11.525$  barn  $\times 6 = 69.15$  barn; Li  $\approx -0.454$  barn  $\times 3 = -1.362$  barn; Y  $\approx 7.55$  barn and In  $\approx 2.08$  barn) and the typical stacking fault disorder in honeycomb-type compounds does not affect the average anion substructure. Accordingly, the neutron diffraction data can be refined with an ordered structural model leading to a satisfying fit for the neutron data (Figure S7a) but to an insufficient fit for the X-ray diffraction data (Figure S4). Therefore, the same two-phase model used for the X-ray powder diffraction data is used for the neutron diffraction data, by fixing all parameters to the values from the X-ray diffraction data and only refining the lithium-ion occupancies (Figure S7b and S8, S9). This leads to a useful refinement of the two subsets of data, for both the X-ray and neutron powder diffraction.

For the monoclinic phase, the lithium-ions are suggested to occupy octahedral Li(1) and Li(2) positions along with the bridging tetrahedral Li(3) site in the (002) plane and disordered In(2)/Li(4) position) site having In2-Li disorder in the (001) plane.<sup>22</sup> Here, we find a partial occupancy of lithium-ion sites in (002) plane (Li(1), Li(2) and Li(3)), together with occupational disorder on In(2)/Li(4) site, as seen in Figure 6b. Partial occupation of lithium-ion indicates a three dimensional lithium-ion diffusion pathway in monoclinic Li<sub>3</sub>Y<sub>1-x</sub>In<sub>x</sub>Cl<sub>6</sub> resulting in lower activation energy and enhanced ionic conductivity. However, no direct link can be found between the indium stoichiometry, stacking fault content and lithium-ion occupancy. Moreover, a complete structural information cannot be obtained, since TOPAS averages the stacking fault, and the refined structures stays in the chosen *P*1 symmetry. Therefore, only the refinement results from the X-ray diffraction data are fully tabulated as an in-depth data analysis regarding to the complexity of the samples (disordered and ordered domains, etc.) does not allow for this using neutron diffraction.

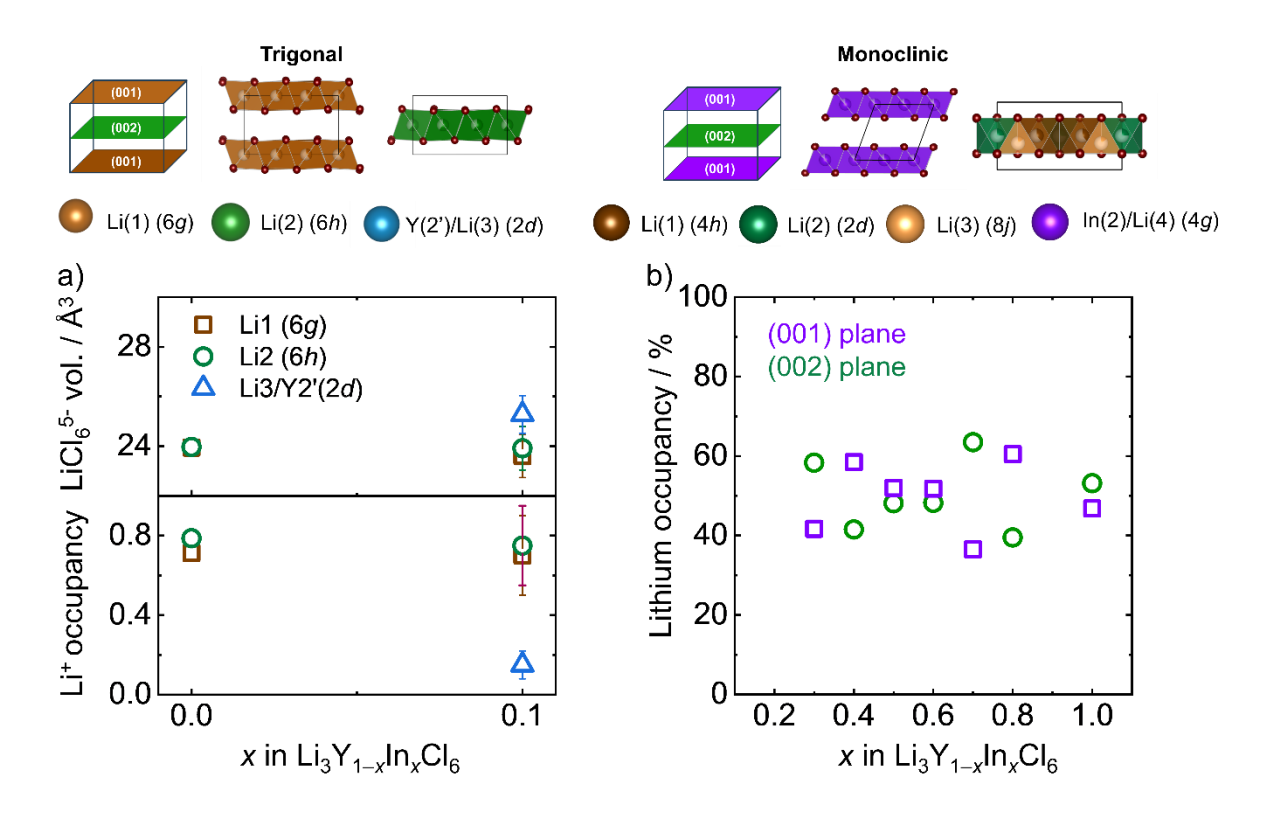


**Figure 6.** The layered structure of the trigonal and monoclinic unit cell can be understood from the schematic showing the (001) and (002) planes. The Rietveld refinement was performed on the neutron powder diffraction data of  $\text{Li}_3\text{Y}_{1-x}\text{In}_x\text{Cl}_6$  with x=0.1 since it crystallizes in the ordered trigonal  $\text{Li}_3\text{YCl}_6$  structure. a)  $(\text{LiCl}_6)^{5-}$  volume (top part) and occupancy (bottom part) changes upon indium substitution within the trigonal phase. b) The lithium-ion occupancy in (001) and (002) planes of the monoclinic phase shows random distribution of lithium-ion over rising indium content.  $\text{Li}_3\text{Y}_{1-x}\text{In}_x\text{Cl}_6$  with  $0.3 \le x \le 1.0$  is a mixture of ordered monoclinic phase along with stacking faulted monoclinic phase. Hence, the two-phase refinement model was adopted to evaluate the lithium-ion distribution between (001) and (002) planes from the neutron powder diffraction.

## **Solid-state NMR**

<sup>6</sup>Li MAS NMR. Qualitative comparison between chemical environments around Lithium-ion in different compounds was performed using <sup>6</sup>Li MAS NMR, (spin quantum number I = 1) as <sup>6</sup>Li has significantly lower broadening effects from magnetic dipole-dipole and 1<sup>st</sup>/2<sup>nd</sup> order electric quadrupolar couplings leading to improved spectral resolution. <sup>66</sup> As seen in Figure 7a, <sup>6</sup>Li signals from Li-ions in the trigonal phase were centered around –0.91 ppm and –0.87 ppm for x = 0.1 and 0.2, respectively. The asymmetric nature of the <sup>6</sup>Li peaks are associated with

the different chemical environment surrounding the lithium-ions and can be correlated with the presence of different lithium-ion Wyckoff sites, (Li(1), Y(2')/Li(3) in (001) plane and Li(2) in (002) plane, see Figure S10a), as confirmed by the Rietveld refinement of the neutron diffraction.

The  $^6$ Li MAS NMR spectrum of monoclinic Li<sub>3</sub>InCl<sub>6</sub> contains two  $^6$ Li signals (centered around -0.67 ppm and -0.71 ppm) – these signals have been attributed to lithium-ion present in (002) plane (Li(1), Li(2), Li(3)) and (001) plane (In(2)/Li(4)) layers, respectively, see Figure S10b. For the monoclinic phase with the composition  $0.3 \le x \le 0.9$ , the most intense  $^6$ Li signal position varies between -0.64 ppm to -0.68 ppm. Unavailability of information on distribution of individual  $^6$ Li crystallographic sites in (002) plane due to structural complexity (coming from large degree of stacking faults) inhibits us from further assignment of the  $^6$ Li signals to any crystallographic lithium-ion sites. While the structural complexity makes it quite difficult to correlate the  $^6$ Li chemical shifts with substitution degree, an observable broadening of the most intense signal does occur for 0.3 < x < 0.9 of the monoclinic phase, indicating greater amount of disorder present in these samples. For x = 0.5, the broadest asymmetric  $^6$ Li signal was observed suggesting that a random distribution of Li-ion environments in the sample is present, probably due to a larger degree of stacking faults<sup>39</sup>.

 $^7Li$  spin-lattice ( $T_1$ ) relaxation. The MHz-regime dynamics of mobile lithium-ion in local ( $10^{-10}$  to  $10^{-9}$  m) scale can be probed using  $^7Li$  spin-lattice ( $T_1$ ) relaxometry.  $^{66,67}$  For the samples with x = 0.3–0.9 (except for 0.5), two rate maxima are visible in the  $T_1$ -relaxation data, (Figure 7b, S11 and S12a; note that the data are displayed as  $\ln(1/T_1)$  corresponding to the relaxation rates) indicating two distinct ionic jump processes. A similar behavior has been observed and reported for several lithium-ion conductors.  $^{22,32,68}$  Epp *et al.* had attributed the different rate peaks to two distinct and fast dynamic processes of lithium-ion hopping in  $Li_{1.5}Al_{0.5}Ti_{1.5}(PO_4)_3$ . For a similar substitution series based on  $Li_{3-x}In_{1-x}Zr_xCl_6$ , Helm *et al.* also observed two dynamical modes in  $^7Li$   $T_1$ -relaxation for x = 0.0 and 0.1 at higher temperature. With higher Zr-content, the high temperature mode gradually approached the low temperature one, leading to single rate peak for x > 0.1. In a recent study, van der Maas *et al.* re-investigated the  $Li_{3-x}In_{1-x}Zr_xCl_6$  series in detail using  $^{6,7}Li$   $T_1$ -relaxation measurement at multiple Larmor frequencies. Here, also two-maxima rate curves were observed, where the faster and slower jump processes were assigned to jumps within the lithium-ion-only layer (*ab* plane) and along c-axis, respectively. For trigonal  $Li_3YCl_6$  with stacking faults, Sebti *et al.* also

observed two slower diffusing components via pulsed field gradient-NMR (PFG-NMR) and attributed them to in-plane (*ab*-plane) and out-of-plane (along *c*-axis) Li-ion diffusion.<sup>39</sup>

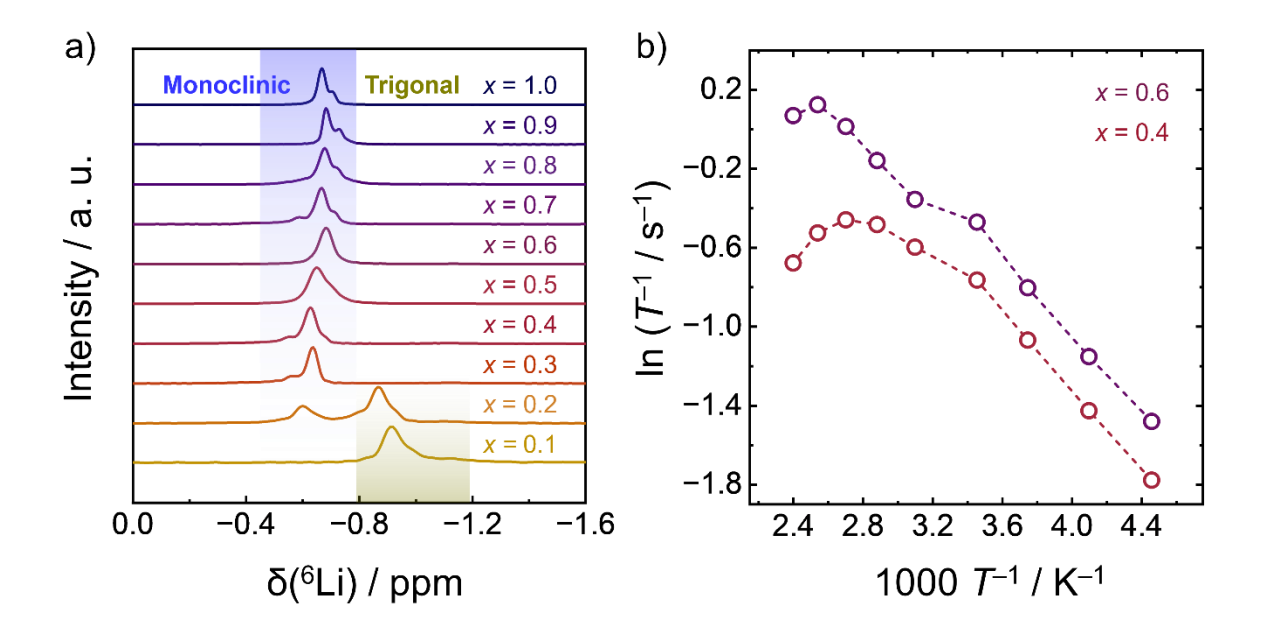


**Figure 7.** a)  $^6$ Li MAS NMR spectra of Li<sub>3</sub>Y<sub>1-x</sub>In<sub>x</sub>Cl<sub>6</sub> with x = 0.1-1.0, measured at ambient temperature and spinning frequency of 12.5 kHz. b) Arrhenius plot of  $^7$ Li  $T_1$ -relaxation measurements for Li<sub>3</sub>Y<sub>1-x</sub>In<sub>x</sub>Cl<sub>6</sub> with x = 0.4 and 0.6 obtained via a saturation recovery experiment. Dashed lines indicate guide-to-eye.

Based on the detailed work by van der Maas  $et\ al.$  with the same parent material Li<sub>3</sub>InCl<sub>6</sub>, the presence of two rate maxima in the  $^7$ Li-relaxation curves in Figure 7b might be associated with lithium-ion-jump processes in the ab-plane and along c-axis in the monoclinic phase. Qualitative comparison of  $^7$ Li-relaxation curves (Figure S11 and S12) indicates that the position and separation between the peaks (if present) are possibly a result of complex interplay between their local structure, relative amount of faulted phase present and their overall ionic conductivity. However, a quantitative analysis of jump processes via fitting the  $T_1$ -relaxation data to accommodate the two different rate peaks observed is not possible because of insufficient number of high-temperature data points after the peak maxima.

For Li<sub>3</sub>InCl<sub>6</sub>, we fitted the corresponding  $^7$ Li  $T_1$ -relaxation data (Figure S12b) using four different models used by van der Maas *et al.*<sup>32</sup> for a comparison of NMR relaxation behavior corresponding to a Larmor frequency of 116 MHz. Similar to the previous report, better fits were observed using the two empirical models (i.e. modified BPP model for 3D motion and modified Richardson model for 2D motion), see Figure S13. However, the choice and

interpretation of the fitting models becomes severely complex considering the simultaneous effect of dimensionality and correlations due to coulomb interactions present in such systems<sup>32</sup>. A detailed investigation is beyond the scope of this work considering the structural complexity due to layered disorder present in our sample combined with our hardware limitation. The best fit was obtained with the modified BPP formula<sup>69</sup> with  $\beta = 0.76$  (a correction exponent incorporated in BPP formula for application in ionic translation in solids<sup>70</sup>) and an activation energy  $E_{\rm a, NMR} = 0.17 \, {\rm eV}$ .

## **Ionic transport**

The ionic conductivities for the herein investigated Li<sub>3</sub>Y<sub>1-x</sub>In<sub>x</sub>Cl<sub>6</sub> samples with  $x \ge 0.1$  are determined from temperature-dependent impedance spectroscopy. As previously shown, the room-temperature conductivity increases with the indium concentration.<sup>29</sup> Representative Nyquist plots at 298 K are shown in Figure S14. In general, the low-temperature impedance spectra show a suppressed semicircle and a capacitive blocking behavior of the electrodes (Figure S15a). To fit the temperature-dependent impedance spectra, an equivalent circuit model (see the inset of Figure S15a) consisting of a parallel resistor and a constant-phase element (CPE) in series with the CPE - representing combined bulk and grain boundary processes as well as the blocking electrodes - is used. In the impedance spectra of the monoclinic phase recorded at elevated temperatures, only the capacitive behavior of the electrodes was fit due to high conductivity, as seen in Figure S15b for the Li<sub>3</sub>Y<sub>1-x</sub>In<sub>x</sub>Cl<sub>6</sub> with x = 0.7. Low values of the ideality factors (0.62 to 0.75) of the constant phase element suggests the presence of more than one process in the trigonal phase, e.g., bulk, grain boundary, which cannot be properly resolved.<sup>71</sup> An Arrhenius behavior can be observed for all the compositions and the activation energy can be obtained from a linear fit (Figure 8a).

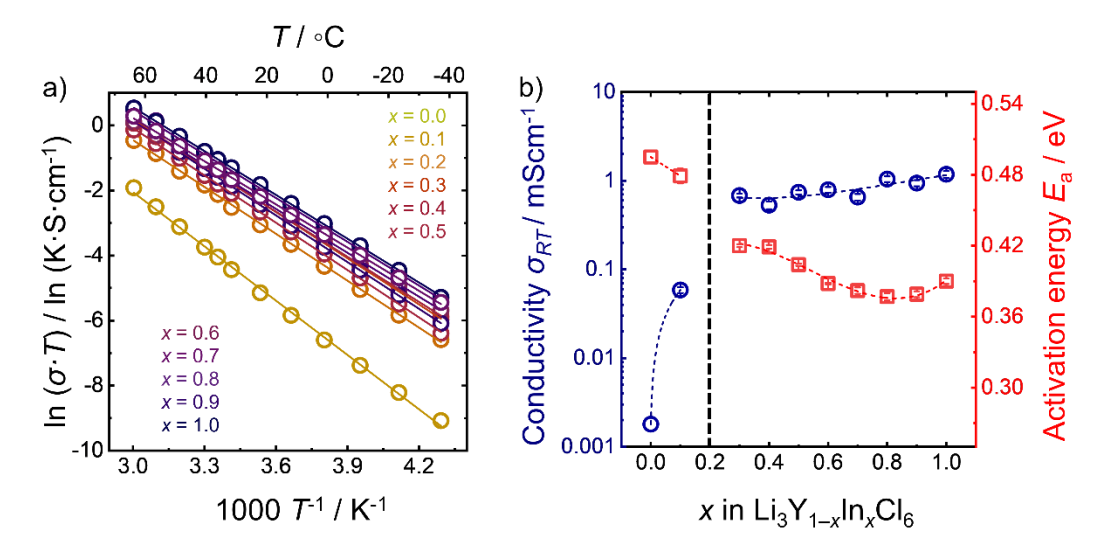


**Figure 8.** a) Temperature-dependent ionic conductivity for the Li<sub>3</sub>Y<sub>1-x</sub>In<sub>x</sub>Cl<sub>6</sub> substitution series following Arrhenius relation, represented by solid lines. b) Room-temperature conductivity and activation energy for all the compositions as a function of indium content. Dotted lines indicate guide-to-eye for b).

The introduction of indium shows beneficial effects on the ionic transport properties of Li<sub>3</sub>YCl<sub>6</sub>. A sharp change in conductivity is visible from x = 0.1 to x = 0.3, corresponding to trigonal to monoclinic phase transition (Figure 8a and b). A similar trend is visible in the activation energy. The pristine trigonal Li<sub>3</sub>YCl<sub>6</sub> has an activation energy of 0.49 eV,<sup>20</sup> which decreases with indium substitution. Upon the structural change, a rapid drop in activation energy can be observed. The monoclinic Li<sub>3</sub>Y<sub>0.3</sub>In<sub>0.7</sub>Cl<sub>6</sub> shows an activation energy of 0.380(1) eV. Previously, Li<sub>3</sub>Y<sub>1-x</sub>In<sub>x</sub>Cl<sub>6</sub> was synthesized via ball milling followed by annealing.<sup>29</sup> A room temperature ionic conductivity of 1.42 mScm<sup>-1</sup> and an activation energy of ~0.32 eV was observed for Li<sub>3</sub>InCl<sub>6</sub>. The deviation of conductivity and activation energy as compared to the previous reports can be attributed to difference in the synthesis process<sup>68</sup> along with inter-laboratory measurement difference.<sup>72</sup>

In general, an increasing indium content in the monoclinic Li<sub>3</sub>Y<sub>1-x</sub>In<sub>x</sub>Cl<sub>6</sub> leads to a minute increase in the ionic conductivity (Figure 8b, blue line and symbols) associated with a small drop in the activation energy (Figure 8b, red line and symbols). Even though the degree of stacking fault varies in the range between 0.2 < x < 1.0 (Figure S17), the change of the conductivity is minor. In contrast, the activation energy decreases showing a small drop with increasing indium content in the monoclinic phase. This may be associated with the substitution of the larger yttrium-ion with the smaller indium-ion (Figure 8b, blue line and symbols). We have estimated the pre-exponential factors for all the compositions from the substitution series

(Figure S18). However, it cannot be directly correlated to the entropic factor and associated structural disorder. This is probably because of the complex correlation of structural parameters and fault content with the transport properties. Although short range lithium-ion diffusion may become more facile with stacking-disorder,<sup>39</sup> the stacking fault disorder seems to not have a major impact on the average long range ionic conductivity here. This was already observed for isostructural lithium rare-earth metal bromides and iodides<sup>40</sup> and may originate in the fact that this type of disorder does not alter the long-range connectivity of (LiCl<sub>6</sub>)<sup>5-</sup> octahedra and therefore the average ion migration paths.

#### 4. Discussion

In the investigated  $\text{Li}_3\text{Y}_{1-x}\text{In}_x\text{Cl}_6$  substitution series, general trends can be found regarding the systematic increase of indium content in the structure:

- 1. The Li<sub>3</sub>Y<sub>1-x</sub>In<sub>x</sub>Cl<sub>6</sub> series exhibits a broad structural diversity. Li<sub>3</sub>YCl<sub>6</sub> crystallizes in a trigonal structure whereas Li<sub>3</sub>InCl<sub>6</sub> is monoclinic. A transformation from a trigonal to a monoclinic phase via an orthorhombic phase is visible in the diffraction patterns of the Li<sub>3</sub>Y<sub>1-x</sub>In<sub>x</sub>Cl<sub>6</sub> series. Li<sub>3</sub>Y<sub>0.9</sub>In<sub>0.1</sub>Cl<sub>6</sub> crystallizes in an ordered trigonal structure and a further increase in the indium content changes the structure from trigonal to orthorhombic to monoclinic phase with a layered honeycomb motif. The monoclinic phases show intergrown domains of randomly oriented honeycomb layers (i.e. stacking faulted layers) and faultless stacked honeycomb layers.
- 2. The degree of stacking fault formation changes significantly depending on the crystal structure and indium content. Although a similar temperature profile in the synthesis is used for  $\text{Li}_3\text{Y}_{1-x}\text{In}_x\text{Cl}_6$  with  $0.1 \le x \le 0.7$ , trigonal  $\text{Li}_3\text{Y}_{0.9}\text{In}_{0.1}\text{Cl}_6$  does not show any indication of stacking fault formation. However, a large percentage of faulted phase is observed in the monoclinic  $\text{Li}_3\text{Y}_{1-x}\text{In}_x\text{Cl}_6$ . Further investigation to explore the influence of synthesis on the crystal structure and with it the stacking fault formation may help to design single phase halide ion conductors needed to study the structural influence on the ion transport in layered ternary halides.
- 3. The lack of observed stacking faults in the neutron data might be a strong indication of cation ordering and stacking fault formation rather than the anion network that contributes to the observed phenomenon. Hence, only neutron diffraction data might not be always helpful to understand the lithium-substructure and diffusion pathway in

these materials. Moreover, it may mislead the analysis via averaging the presence of multiphase faulted mixture with M/Li-disorder. Hence, a combination of X-ray and neutron powder diffraction is necessary for a deeper phase analysis of lithium-ion conducting ternary halides. For in-depth systematic structural analysis and structure-property correlation, unfortunately, stacking fault models is needed.

- 4. Li<sub>3</sub>InCl<sub>6</sub> in the monoclinic phase in known to have two different indium sites, In1 (2*a*) and In2 (4*g*) on the (001) plan of the unit cell. In addition to the three lithium sites on (002) plane, lithium forms disorder with indium on the 4*g* Wyckoff site. In2 and Li<sup>4</sup> occupancy 4*g* site of Li<sub>3</sub>InCl<sub>6</sub> are 0.5 and 0.39, respectively<sup>22</sup>. However, the stacking disorder and site disorder were not deconvoluted previously because of structural complexity. Additionally, due to the "two phase" character, an intralayer disorder correlates with the phase fraction to 100 %. Hence it is impossible to deconvolute the anti-site defect and stacking fault for the current substitution series.
- 5. With the increase in indium content, the *hcp* anionic framework structure transforms to a *ccp* framework leading to a trigonal-to-monoclinic phase transition. For the monoclinic phase, the lattice volume is much higher than that of trigonal one. A sharp drop in activation energy and increase in ionic conductivity is observed, as seen in Figure 8b, which can be attributed to increment in lattice volume leading to widen of lithium-ion diffusion pathway during the phase change. The higher conductivity in the monoclinic phase also correlates with the occupation of the tetrahedral sites by lithiumion in the (002) plane (and of course the fractional occupation), which suggests that such sites are energetically accessible and connect the lithium-ion diffusion pathways in and perhaps also out-of plane.

#### 6. Conclusions

In summary, we have investigated the phase evolution and ionic transport properties of the  $\text{Li}_3\text{Y}_{1-x}\text{In}_x\text{Cl}_6$  substitution series via X-ray and neutron powder diffraction, temperature-dependent impedance measurement, <sup>7</sup>Li spin-lattice relaxation measurement and <sup>6</sup>Li magicangle spinning nuclear magnetic resonance. Along with the known 6g and 6h lithium-ion sites for trigonal  $\text{Li}_3\text{YCl}_6$ , lithium-ion occupies 2d sites in the (001) plane for x = 0.1 leading to improved transport. In addition to a structural transformation with increasing indium content, two-dimensional stacking fault defects are found in the monoclinic  $\text{Li}_3\text{Y}_{1-x}\text{In}_x\text{Cl}_6$  phase for  $x \ge 0.2$ . A complete phase analysis is only possible by refining X-ray powder diffraction data using

a two-phase model including a faultless and faulted polytype with randomly oriented metal, M bearing cation layers. Here, the indium content seems to affect the ratio of faulted to ordered phase showing a maximum faulting for Li<sub>3</sub>Y<sub>0.5</sub>In<sub>0.5</sub>Cl<sub>6</sub>. Since, it is challenging to extract in depth structural information due to the multiphase disordered nature of the Li<sub>3</sub>Y<sub>1-x</sub>In<sub>x</sub>Cl<sub>6</sub> for  $x \ge 0.2$ , we used neutron diffraction only to find out the lithium-ion distribution in the (001) and (002) plane. The phase analysis along with temperature dependent ionic conductivity measurement confirms a strong influence of the symmetry of the structure/the structure type (i.e. trigonal vs monoclinic); however, the stacking faults overall do not seem to have a dominant influence on the lithium-ion transport. This study further hints on the strong impact of substitution and crystal structure on the stacking fault formation in this class of materials. Nevertheless, it shows that despite the differences in faulting, the overall ionic conductivity remains unaffected.

#### **Associated Content**

## **Supporting Information**

X-ray and neutron powder diffraction data with corresponding fit models and refinement parameter details for all the compositions, ,  $^6$ Li MAS NMR data with corresponding fit for x = 0.1 and 1.0, Arrhenius plot of  $^7$ Li  $T_1$ -relaxation measurements for Li<sub>3</sub>Y<sub>1-x</sub>In<sub>x</sub>Cl<sub>6</sub> with x = 0.3-1.0, fit of  $^7$ Li  $T_1$ -relaxation data for x = 1.0 using four different models, Nyquist plots of impedance data for monoclinic Li<sub>3</sub>Y<sub>1-x</sub>In<sub>x</sub>Cl<sub>6</sub> samples with x = 0.1-1.0 at 298 K, temperature dependent Nyquist plots of impedance data for monoclinic Li<sub>3</sub>Y<sub>1-x</sub>In<sub>x</sub>Cl<sub>6</sub> with x = 0.7 sample, pre-factor data, trigonal-orthorhombic-monoclinic phase evolution, ratio of faulted to unfaulted phase. 'PDF'

#### **Notes**

Authors declare no competing financial interest.

## Acknowledgements

The research was supported by the Federal Ministry of Education and Research (BMBF) within project FESTBATT under grant number 03XP0430F. We further acknowledge funding from

the Deutsche Forschungsgemeinschaft under project number 459785385. A. B. acknowledges the Alexander von Humboldt Foundation for the financial support through a Postdoctoral Fellowship. B.S. is a member of the International Graduate School for Battery Chemistry, Characterization, Analysis, Recycling and Application (BACCARA), which is funded by the Ministry for Culture and Science of North Rhine-Westphalia, Germany. A portion of this research used resources at the the Spallation Neutron Source, a DOE Office of Science User Facility operated by the Oak Ridge National Laboratory.

#### References

- (1) Janek, J.; Zeier, W. G. A Solid Future for Battery Development. *Nat. Energy* **2016**, *1* (9), 16141. https://doi.org/10.1038/nenergy.2016.141.
- (2) Murugan, R.; Thangadurai, V.; Weppner, W. Fast Lithium Ion Conduction in Garnet-Type  $\text{Li}_7\text{La}_3\text{Zr}_2\text{O}_{12}$ . Angew. Chem., Int. Ed. Engl. **2007**, 46 (41), 7778–7781. https://doi.org/10.1002/anie.200701144.
- (3) Lu, Y.; Meng, X.; Alonso, J. A.; Fernández-Díaz, M. T.; Sun, C. Effects of Fluorine Doping on Structural and Electrochemical Properties of Li<sub>6.25</sub>Ga<sub>0.25</sub>La<sub>3</sub>Zr<sub>2</sub>O<sub>12</sub> as Electrolytes for Solid-State Lithium Batteries. *ACS Appl. Mater. Interfaces* **2019**, *11* (2), 2042–2049. https://doi.org/10.1021/acsami.8b17656.
- (4) Deng, Y.; Eames, C.; Fleutot, B.; David, R.; Chotard, J. N.; Suard, E.; Masquelier, C.; Islam, M. S. Enhancing the Lithium Ion Conductivity in Lithium Superionic Conductor (LISICON) Solid Electrolytes through a Mixed Polyanion Effect. *ACS Appl. Mater. Interfaces* **2017**, *9* (8), 7050–7058. https://doi.org/10.1021/acsami.6b14402.
- (5) Kanno, R.; Murayama, M. Lithium Ionic Conductor Thio-LISICON: The Li<sub>2</sub>S-GeS<sub>2</sub>-P<sub>2</sub>S<sub>5</sub> System. *J. Electrochem. Soc.* **2001**, *148* (7), A742. https://doi.org/10.1149/1.1379028.
- (6) Minafra, N.; Hogrefe, K.; Barbon, F.; Helm, B.; Li, C.; Wilkening, H. M. R.; Zeier, W. G. Two-Dimensional Substitution: Toward a Better Understanding of the Structure-Transport Correlations in the Li-Superionic Thio-LISICONs. *Chem. Mater.* **2021**, *33* (2), 727–740. https://doi.org/10.1021/acs.chemmater.0c04150.
- (7) Kato, Y.; Saito, R.; Sakano, M.; Mitsui, A.; Hirayama, M.; Kanno, R. Synthesis, Structure and Lithium Ionic Conductivity of Solid Solutions of Li<sub>10</sub>(Ge<sub>1-x</sub>M<sub>x</sub>)P<sub>2</sub>S<sub>12</sub> (M = Si, Sn). J. Power Sources **2014**, 271, 60–64. https://doi.org/10.1016/j.jpowsour.2014.07.159.
- (8) Kato, Y.; Hori, S.; Saito, T.; Suzuki, K.; Hirayama, M.; Mitsui, A.; Yonemura, M.; Iba, H.; Kanno, R. High-Power All-Solid-State Batteries Using Sulfide Superionic Conductors. *Nat. Energy* **2016**, *1* (4), 16030. https://doi.org/10.1038/nenergy.2016.30.
- (9) Kraft, M. A.; Culver, S. P.; Calderon, M.; Böcher, F.; Krauskopf, T.; Senyshyn, A.; Dietrich, C.; Zevalkink, A.; Janek, J.; Zeier, W. G. Influence of Lattice Polarizability on the Ionic Conductivity in the Lithium Superionic Argyrodites Li<sub>6</sub>PS<sub>5</sub>X (X = Cl, Br, I). *J. Am. Chem. Soc.* **2017**, *139* (31), 10909–10918. https://doi.org/10.1021/jacs.7b06327.
- (10) Zhou, L.; Assoud, A.; Zhang, Q.; Wu, X.; Nazar, L. F. New Family of Argyrodite Thioantimonate Lithium Superionic Conductors. *J. Am. Chem. Soc.* **2019**, *141* (48), 19002–19013. https://doi.org/10.1021/jacs.9b08357.
- (11) Culver, S. P.; Koerver, R.; Krauskopf, T.; Zeier, W. G. Designing Ionic Conductors: The Interplay between Structural Phenomena and Interfaces in Thiophosphate-Based Solid-State Batteries. *Chem. Mater.* **2018**, *30* (13), 4179–4192. https://doi.org/10.1021/acs.chemmater.8b01293.
- (12) Zhou, L.; Minafra, N.; Zeier, W. G.; Nazar, L. F. Innovative Approaches to Li-Argyrodite Solid Electrolytes for All-Solid-State Lithium Batteries. *Acc. Chem. Res.* **2021**, *54* (12), 2717–2728. https://doi.org/10.1021/acs.accounts.0c00874.

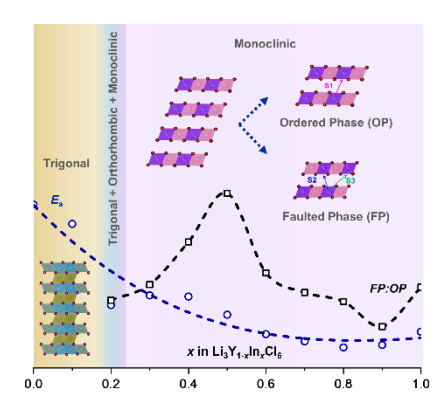
- (13) Li, X.; Liang, J.; Yang, X.; Adair, K. R.; Wang, C.; Zhao, F.; Sun, X. Progress and Perspectives on Halide Lithium Conductors for All-Solid-State Lithium Batteries. *Energy Environ. Sci.* **2020**, *13*, 1429–1461. https://doi.org/10.1039/c9ee03828k.
- (14) Liang, J.; Li, X.; Adair, K. R.; Sun, X. Metal Halide Superionic Conductors for All-Solid-State Batteries. *Acc. Chem. Res.* **2021**, *54* (4), 1023–1033. https://doi.org/10.1021/acs.accounts.0c00762.
- (15) Kwak, H.; Wang, S.; Park, J.; Liu, Y.; Kim, K. T.; Choi, Y.; Mo, Y.; Jung, Y. S. Emerging Halide Superionic Conductors For. *ACS Energy Lett.* **2022**, *7* (5), 1776–1805. https://doi.org/10.1021/acsenergylett.2c00438.
- (16) Zhang, S.; Zhao, F.; Chen, J.; Fu, J.; Luo, J.; Alahakoon, S. H.; Chang, L.; Feng, R.; Shakouri, M. A Family of Oxychloride Amorphous Solid Electrolytes for Long-Cycling All-Solid-State Lithium Batteries. *Nat. Commun.* 2023, 14, 3780. https://doi.org/10.1038/s41467-023-39197-8.
- (17) Tanaka, Y.; Ueno, K.; Mizuno, K.; Takeuchi, K.; Asano, T.; Sakai, A. New Oxyhalide Solid Electrolytes with High Lithium Ionic Conductivity >10 mScm<sup>-1</sup> for All-Solid-State Batteries. *Angew. Chem., Int. Ed. Engl.* **2023**, *62* (13), 1–5. https://doi.org/10.1002/anie.202217581.
- (18) Ginnings, D. C.; Phipps, T. E. Temperature-Conductance curves of Solid Salts. III. Halides of Lithium. *J. Am. Chem. Soc.* **1930**, *52* (4), 1340–1345. https://doi.org/10.1021/ja01367a006.
- (19) Asano, T.; Sakai, A.; Ouchi, S.; Sakaida, M.; Miyazaki, A.; Hasegawa, S. Solid Halide Electrolytes with High Lithium-Ion Conductivity for Application in 4 V Class Bulk-Type All-Solid-State Batteries. *Adv. Mater.* **2018**, *30* (44), 1–7. https://doi.org/10.1002/adma.201803075.
- (20) Schlem, R.; Muy, S.; Prinz, N.; Banik, A.; Shao-Horn, Y.; Zobel, M.; Zeier, W. G. Mechanochemical Synthesis: A Tool to Tune Cation Site Disorder and Ionic Transport Properties of Li<sub>3</sub>*M*Cl<sub>6</sub> (*M* = Y, Er) Superionic Conductors. *Adv. Energy Mater.* **2020**, *10*, 1903719. https://doi.org/10.1002/aenm.201903719.
- (21) Schlem, R.; Bernges, T.; Li, C.; Kraft, M. A.; Minafra, N.; Zeier, W. G. Lattice Dynamical Approach for Finding the Lithium Superionic Conductor Li<sub>3</sub>ErI<sub>6</sub>. *ACS Appl. Energy Mater.* **2020**, *3* (4), 3684–3691. https://doi.org/10.1021/acsaem.0c00147.
- (22) Helm, B.; Schlem, R.; Wankmiller, B.; Banik, A.; Gautam, A.; Ruhl, J.; Li, C.; Hansen, M. R.; Zeier, W. G. Exploring Aliovalent Substitutions in the Lithium Halide Superionic Conductor  $\text{Li}_{3\text{-x}}\text{In}_{1\text{----}} _x\text{Zr}_x\text{Cl}_6$  (0  $\leq$  x  $\leq$  0.5). *Chem. Mater.* **2021**, 33 (12), 4773–4782. https://doi.org/10.1021/acs.chemmater.1c01348.
- (23) Park, K. H.; Kaup, K.; Assoud, A.; Zhang, Q.; Wu, X.; Nazar, L. F. High-Voltage Superionic Halide Solid Electrolytes for All-Solid-State Li-Ion Batteries. *ACS Energy Lett.* **2020**, 533–539. https://doi.org/10.1021/acsenergylett.9b02599.
- (24) Wang, S.; Bai, Q.; Nolan, A. M.; Liu, Y.; Gong, S.; Sun, Q.; Mo, Y. Lithium Chlorides and Bromides as Promising Solid-State Chemistries for Fast Ion Conductors with Good Electrochemical Stability. *Angew. Chem.*, *Int. Ed. Engl.* **2019**, *58* (24), 8039–8043. https://doi.org/10.1002/anie.201901938.
- (25) Rosenbach, C.; Walther, F.; Ruhl, J.; Hartmann, M.; Hendriks, T. A.; Ohno, S.; Janek, J.; Zeier, W. G. Visualizing the Chemical Incompatibility of Halide and Sulfide-Based Electrolytes in Solid-State Batteries. *Adv. Energy Mater.* **2023**, *13* (6). https://doi.org/10.1002/aenm.202203673.
- (26) Riegger, L. M.; Schlem, R.; Sann, J.; Zeier, W. G.; Janek, J. Lithium-Metal Anode Instability of the Superionic Halide Solid Electrolytes and the Implications for Solid-State Batteries. *Angew. Chem., Int. Ed. Engl.* **2021**, *60* (12), 6718–6723. https://doi.org/10.1002/anie.202015238.
- (27) Koç, T.; Hallot, M.; Quemin, E.; Hennequart, B.; Dugas, R.; Abakumov, A. M.; Lethien, C.; Tarascon, J. M. Toward Optimization of the Chemical/Electrochemical Compatibility of Halide Solid Electrolytes in All-Solid-State Batteries. *ACS Energy Lett.* **2022**, 2979–2987. https://doi.org/10.1021/acsenergylett.2c01668.
- (28) Liu, Z.; Ma, S.; Liu, J.; Xiong, S.; Ma, Y.; Chen, H. High Ionic Conductivity Achieved in Li<sub>3</sub>Y(Br<sub>3</sub>Cl<sub>3</sub>) Mixed Halide Solid Electrolyte via Promoted Diffusion Pathways and Enhanced Grain Boundary. *ACS Energy Lett.* **2021**, *6* (1), 298–304. https://doi.org/10.1021/acsenergylett.0c01690.
- (29) Li, X.; Liang, J.; Adair, K. R.; Li, J.; Li, W.; Zhao, F.; Hu, Y.; Sham, T.-K.; Zhang, L.; Zhao, S.; Lu, S.; Huang, H.; Li, R.; Chen, N.; Sun, X. Origin of Superionic Li<sub>3</sub>Y<sub>1-x</sub>In<sub>x</sub>Cl<sub>6</sub> Halide Solid

- Electrolytes with High Humidity Tolerance. *Nano Lett.* **2020**, 20, 4384–4392. https://doi.org/https://doi.org/10.1021/acs.nanolett.0c01156.
- (30) Plass, M. A.; Bette, S.; Philipp, N.; Moundrakovski, I.; Küster, K.; Dinnebier, R. E.; Lotsch, B. V. Influence of Synthesis and Substitution on the Structure and Ionic Transport Properties of Lithium Rare Earth Metal Halides. *J. Mater. Chem. A* **2023**, *3*, 13027–13038. https://doi.org/10.1039/d3ta01327h.
- (31) Schlem, R.; Banik, A.; Eckardt, M.; Zobel, M.; Zeier, W. G. Na<sub>3-x</sub>Er<sub>1-x</sub>Zr<sub>x</sub>Cl<sub>6</sub> A Halide-Based Fast Sodium-Ion Conductor with Vacancy-Driven Ionic Transport. *ACS Appl. Energy Mater.* **2020**, *3* (10), 10164–10173. https://doi.org/10.1021/acsaem.0c01870.
- (32) Maas, E. van der; Famprikis, T.; Pieters, S.; Dijkstra, J. P.; Li, Z.; Parnell, S. R.; Smith, R. I.; Eck, E. R. H. van; Ganapathy, S.; Wagemaker, M. Re-Investigating the Structure-Property Relationship of the Solid Electrolytes Li<sub>3-x</sub>In<sub>1-x</sub>Zr<sub>x</sub>Cl<sub>6</sub> and the Impact of In-Zr(IV) Substitution. *J. Mater. Chem. A* **2023**, *11* (9), 4559–4571. https://doi.org/10.1039/d2ta08433c.
- (33) Fu, J.; Yang, S.; Hou, J.; Azhari, L.; Yao, Z.; Ma, X.; Liu, Y.; Vanaphuti, P.; Meng, Z.; Yang, Z.; Zhong, Y.; Wang, Y. Modeling Assisted Synthesis of Zr-Doped Li<sub>3-x</sub>In<sub>1-x</sub>Zr<sub>x</sub>Cl<sub>6</sub> with Ultrahigh Ionic Conductivity for Lithium-Ion Batteries. *J. Power Sources* **2023**, *556*, 232465. https://doi.org/10.1016/j.jpowsour.2022.232465.
- (34) Li, X.; Liang, J.; Chen, N.; Luo, J.; Adair, K. R.; Wang, C.; Banis, M. N.; Sham, T. K.; Zhang, L.; Zhao, S.; Lu, S.; Huang, H.; Li, R.; Sun, X. Water-Mediated Synthesis of a Superionic Halide Solid Electrolyte. *Angew. Chem., Int. Ed. Engl.* **2019**, *58* (46), 16427–16432. https://doi.org/10.1002/anie.201909805.
- (35) Wang, C.; Liang, J.; Luo, J.; Liu, J.; Li, X.; Zhao, F.; Li, R.; Huang, H.; Zhao, S.; Zhang, L.; Wang, J.; Sun, X. A Universal Wet-Chemistry Synthesis of Solid-State Halide Electrolytes for All-Solid-State Lithium-Metal Batteries. *Sci. Adv.* **2021**, *7* (37), eabh1896. https://doi.org/10.1126/sciadv.abh1896.
- (36) Schlem, R.; Banik, A.; Ohno, S.; Suard, E.; Zeier, W. G. Insights into the Lithium Sub-Structure of Superionic Conductors Li<sub>3</sub>YCl<sub>6</sub> and Li<sub>3</sub>YBr<sub>6</sub>. *Chem. Mater.* **2021**, *33* (1), 327–337. https://doi.org/10.1021/acs.chemmater.0c04352.
- (37) Ito, H.; Shitara, K.; Wang, Y.; Fujii, K.; Yashima, M.; Goto, Y.; Moriyoshi, C.; Rosero-Navarro, N. C.; Miura, A.; Tadanaga, K. Kinetically Stabilized Cation Arrangement in Li<sub>3</sub>YCl<sub>6</sub> Superionic Conductor during Solid-State Reaction. *Adv. Sci.* **2021**, 8 (15), 1–8. https://doi.org/10.1002/advs.202101413.
- (38) Kwak, H.; Han, D.; Lyoo, J.; Park, J.; Jung, S. H.; Han, Y.; Kwon, G.; Kim, H.; Hong Seung-Tae; Nam Kyung-Wan; Jung, Y. S. New Cost-Effective Halide Solid Electrolytes for All-Solid-State Batteries. *Adv. Energy Mater.* **2021**, *11*, 2003190. https://doi.org/10.1002/aenm.202003190.
- (39) Sebti, E.; Evans, H. A.; Chen, H.; Richardson, P. M.; White, K. M.; Giovine, R.; Koirala, K. P.; Xu, Y.; Gonzalez-Correa, E.; Wang, C.; Brown, C. M.; Cheetham, A. K.; Canepa, P.; Clément, R. J. Stacking Faults Assist Lithium-Ion Conduction in a Halide-Based Superionic Conductor. *J. Am. Chem. Soc.* **2022**, *144* (13), 5795–5811. https://doi.org/10.1021/jacs.1c11335.
- (40) Plass, M. A.; Bette, S.; Dinnebier, R. E.; Lotsch, B. V. Enhancement of Superionic Conductivity by Halide Substitution in Strongly Stacking Faulted Li<sub>3</sub>HoBr<sub>6-x</sub>I<sub>x</sub> Phases. *Chem. Mater.* **2022**, 34 (7), 3227–3235. https://doi.org/10.1021/acs.chemmater.2c00024.
- (41) Bohnsack, A.; Stenzel, F.; Zajonc, A.; Balzer, G.; Wickleder, M. S.; Meyer, G. Ternary Halides of the A<sub>3</sub>MX<sub>6</sub> Type. VI. Ternary Chlorides of the Rare-Earth Elements with Lithium, Li<sub>3</sub>MCI<sub>6</sub> (M = Tb-Lu, Y, Sc): Synthesis, Crystal Structures, and Ionic Motion. *Z. Anorg. Allg. Chem.* **1997**, *623*, 1067–1073. https://doi.org/10.1002/zaac.19976230710.
- (42) Steiner, H.-J.; Lutz, H. D. Novel Fast Ion Conductors of the Type  $M_3^IMCl_6$  ( $M^I$  = Li, Na, Ag;  $M^{III}$  = In, Y). Z. anorg. allg. Chem. **1992**, 613, 26–30. https://doi.org/10.1002/zaac.19926130104.
- (43) Paulsen, J. M.; Mueller-Neuhaus, J. R.; Dahn, J. R. Layered LiCoO2 with a Different Oxygen Stacking (O2 Structure) as a Cathode Material for Rechargeable Lithium Batteries. *J. Electrochem. Soc.* **2000**, *147* (2), 508. https://doi.org/10.1149/1.1393225.

- (44) Jiang, M.; Key, B.; Meng, Y. S.; Grey, C. P. Electrochemical and Structural Study of the Layered, "Li-Excess" Lithium-Ion Battery Electrode Material Li[Li<sub>1/9</sub>Ni<sub>1/3</sub>Mn<sub>5/9</sub>]O<sub>2</sub>. *Chem. Mater.* **2009**, *21* (13), 2733–2745. https://doi.org/10.1021/cm900279u.
- (45) Kitagawa, K.; Takayama, T.; Matsumoto, Y.; Kato, A.; Takano, R.; Kishimoto, Y.; Bette, S.; Dinnebier, R.; Jackeli, G.; Takagi, H. A Spin-Orbital-Entangled Quantum Liquid on a Honeycomb Lattice. *Nature* **2018**, *554* (7692), 341–345. https://doi.org/10.1038/nature25482.
- (46) Bette, S.; Takayama, T.; Kitagawa, K.; Takano, R.; Takagi, H.; Dinnebier, R. E. Solution of the Heavily Stacking Faulted Crystal Structure of the Honeycomb Iridate H<sub>3</sub>LiIr<sub>2</sub>O<sub>6</sub>. *Dalton Trans*. **2017**, *46* (44), 15216–15227. https://doi.org/10.1039/c7dt02978k.
- (47) Bette, S.; Takayama, T.; Duppel, V.; Poulain, A.; Takagi, H.; Dinnebier, R. E. Crystal Structure and Stacking Faults in the Layered Honeycomb, Delafossite-Type Materials Ag<sub>3</sub>LiIr<sub>2</sub>O<sub>6</sub> and Ag<sub>3</sub>LiRu<sub>2</sub>O<sub>6</sub>. *Dalton Trans.* **2019**, *48* (25), 9250–9259. https://doi.org/10.1039/c9dt01789e.
- (48) Coelho, A. A. TOPAS and TOPAS-Academic: An Optimization Program Integrating Computer Algebra and Crystallographic Objects Written in C++: An. *J. Appl. Crystallogr.* **2018**, *51* (1), 210–218. https://doi.org/10.1107/S1600576718000183.
- (49) Cheary, R. W.; Coelho, A. Fundamental Parameters Approach to X-Ray Line-Profile Fitting. *J. Appl. Crystallogr.* **1992**, 25 (pt 2), 109–121. https://doi.org/10.1107/S0021889891010804.
- (50) Cheary, R. W.; Coelho, A. A.; Cline, J. P. Fundamental Parameters Line Profile Fitting in Laboratory Diffractometers. *J. Res. Natl. Inst. Stand. Technol.* **2004**, *109* (1), 1–25. https://doi.org/10.6028/jres.109.002.
- (51) Pawley, G. S. Unit-Cell Refinement from Powder Diffraction Scans. *J. Appl. Crystallogr.* **1981**, *14* (6), 357–361. https://doi.org/10.1107/s0021889881009618.
- (52) Schmidt, M. O.; Wickleder, M. S.; Meyer, G. Ternary Halides of the  $A_3MX_6$  Type. VIII On the Crystal Structure of  $Li_3InCl_6$ . Z. anorg. allg. Chem. **1999**, 625 (6), 539–540. https://doi.org/https://doi.org/10.1002/(SICI)1521-3749(199904)625:4<539::AID-ZAAC539>3.0.CO;2-J.
- (53) Ainsworth, C. M.; Lewis, J. W.; Wang, C. H.; Coelho, A. A.; Johnston, H. E.; Brand, H. E. A.; Evans, J. S. O. 3D Transition Metal Ordering and Rietveld Stacking Fault Quantification in the New Oxychalcogenides La<sub>2</sub>O<sub>2</sub>Cu<sub>2-4x</sub>Cd<sub>2x</sub>Se<sub>2</sub>. *Chem Mater* **2016**, 28 (9), 3184–3195. https://doi.org/10.1021/acs.chemmater.6b00924.
- (54) Coelho, A. A.; Evans, J. S. O.; Lewis, J. W. Averaging the Intensity of Many-Layered Structures for Accurate Stacking-Fault Analysis Using Rietveld Refinement. *J. Appl. Crystallogr.* **2016**, *49* (5), 1740–1749. https://doi.org/10.1107/S1600576716013066.
- (55) Huq, A.; Kirkham, M.; Peterson, P. F.; Hodges, J. P.; Whitfield, P. S.; Page, K.; Hugle, T.; Iverson, E. B.; Parizzia, A.; Rennichb, G. POWGEN: Rebuild of a Third-Generation Powder Diffractometer at the Spallation Neutron Source. *J. Appl. Crystallogr.* **2019**, *52*, 1189–1201. https://doi.org/10.1107/S160057671901121X.
- (56) Van Geet, A. L. Calibration of the Methanol and Glycol Nuclear Magnetic Resonance Thermometers with a Static Thermistor Probe. *Anal. Chem.* **1968**, *40*, 2227–2229. https://doi.org/https://doi.org/10.1021/ac50158a064.
- (57) Zhang, W.; Weber, D. A.; Weigand, H.; Arlt, T.; Manke, I.; Schröder, D.; Koerver, R.; Leichtweiss, T.; Hartmann, P.; Zeier, W. G.; Janek, J. Interfacial Processes and Influence of Composite Cathode Microstructure Controlling the Performance of All-Solid-State Lithium Batteries. *ACS Appl. Mater. Interfaces* **2017**, *9* (21), 17835–17845. https://doi.org/10.1021/acsami.7b01137.
- (58) Shannon, R. D. Revised Effective Ionic Radii and Systematic Studies of Interatomic Distances in Halides and Chalcogenides. *Acta Crystallogr.*, *Sect. A* **1976**, *32* (5), 751–767. https://doi.org/10.1107/S0567739476001551.
- (59) Warren, B. E. X-Ray Diffraction in Random Layer Lattices. *Phys. Rev.* **1941**, *59* (9), 693–698. https://doi.org/10.1103/PhysRev.59.693.
- (60) Welberry, T. R.; Butler, B. D. Interpretation of Diffuse X-Ray Scattering via Models of Disorder. *J. Appl. Crystallogr.* **1994**, 27 (pt 3), 205–231. https://doi.org/10.1107/S0021889893011392.

- (61) Kimber, S. A. J.; Ling, C. D.; Morris, D. J. P.; Chemseddine, A.; Henry, P. F.; Argyriou, D. N. Interlayer Tuning of Electronic and Magnetic Properties in Honeycomb Ordered Ag<sub>3</sub>LiRu<sub>2</sub>O<sub>6</sub>. J. Mater. Chem. 2010, 20 (37), 8021–8025. https://doi.org/10.1039/c0jm00678e.
- (62) Wallace, D. C.; McQueen, T. M. New Honeycomb Iridium(V) Oxides: NaIrO<sub>3</sub> and Sr<sub>3</sub>CaIr<sub>2</sub>O<sub>9</sub>. *Dalton Trans.* **2015**, *44* (47), 20344–20351. https://doi.org/10.1039/c5dt03188e.
- (63) Bette, S.; Dinnebier, R. E.; Freyer, D. Structure Solution and Refinement of Stacking-faulted NiCl(OH). *Jnl. Applied Crystallography*. 2015, pp 1706–1718.
- (64) Diehl, L.; Bette, S.; Pielnhofer, F.; Betzler, S.; Moudrakovski, I.; Ozin, G. A.; Dinnebier, R.; Lotsch, B. V. Structure-Directing Lone Pairs: Synthesis and Structural Characterization of SnTiO<sub>3</sub>. *Chem. Mater.* **2018**, *30* (24), 8932–8938. https://doi.org/10.1021/acs.chemmater.8b04261.
- (65) Pielnhofer, F.; Bette, S.; Eger, R.; Duppel, V.; Nuss, J.; Dolle, C.; Dinnebier, R. E.; Lotsch, B. V. The Stacking Faulted Nature of the Narrow Gap Semiconductor Sc<sub>2</sub>Si<sub>2</sub>Te<sub>6</sub>. *Z. Anorg. Allg. Chem.* **2022**, 648 (21). https://doi.org/10.1002/zaac.202200234.
- (66) Hogrefe, K.; Minafra, N.; Hanghofer, I.; Banik, A.; Zeier, W. G.; Wilkening, H. M. R. Opening Diffusion Pathways through Site Disorder: The Interplay of Local Structure and Ion Dynamics in the Solid Electrolyte Li<sub>6+x</sub>P<sub>1-x</sub>Ge<sub>x</sub>S<sub>5</sub>I as Probed by Neutron Diffraction and NMR. *J. Am. Chem. Soc.* **2022**, *144* (4), 1795–1812. https://doi.org/10.1021/jacs.1c11571.
- (67) Kuhn, A.; Kunze, M.; Sreeraj, P.; Wiemhöfer, H. D.; Thangadurai, V.; Wilkening, M.; Heitjans, P. NMR Relaxometry as a Versatile Tool to Study Li Ion Dynamics in Potential Battery Materials. *Solid State Nucl. Magn. Reason.* 2012, 42, 2–8. https://doi.org/10.1016/j.ssnmr.2012.02.001.
- (68) Epp, V.; Ma, Q.; Hammer, E. M.; Tietz, F.; Wilkening, M. Very Fast Bulk Li Ion Diffusivity in Crystalline Li<sub>1.5</sub>Al<sub>0.5</sub>Ti<sub>1.5</sub>(PO<sub>4</sub>)<sub>3</sub> as Seen Using NMR Relaxometry. *Phys. Chem. Chem. Phys.* **2015**, *17* (48), 32115–32121. https://doi.org/10.1039/c5cp05337d.
- (69) Bloembergen, N.; Purcell, E. M.; Pound, R. V. Relaxation Effects in Nuclear Magnetic Resonance Absorption. *Phys. Rev.* **1948**, *73* (7), 679–712. https://doi.org/10.1103/PhysRev.73.679.
- (70) Wankmiller, B.; Hansen, M. R. Observation of Li+ Jumps in Solid Inorganic Electrolytes over a Broad Dynamical Range: A Case Study of the Lithium Phosphidosilicates Li<sub>8</sub>SiP<sub>4</sub> and Li<sub>14</sub>SiP<sub>6</sub>. *J Magn. Reason. Open* **2023**, *14*–*15*. https://doi.org/10.1016/j.jmro.2023.100098.
- (71) Brug, G. J.; van den Eeden, A. L. G.; Sluyters-Rehbach, M.; Sluyters, J. H. The Analysis of Electrode Impedances Complicated by the Presence of a Constant Phase Element. *J. Electroanal. Chem.* **1984**, *176* (1–2), 275–295. https://doi.org/10.1016/S0022-0728(84)80324-1.
- (72) Ohno, S.; Bernges, T.; Buchheim, J.; Duchardt, M.; Hatz, A.-K.; Kraft, M. A.; Kwak, H.; Santhosha, A. L.; Liu, Z.; Minafra, N.; Tsuji, F.; Sakuda, A.; Schlem, R.; Xiong, S.; Zhang, Z.; Adelhelm, P.; Chen, H.; Hayashi, A.; Jung, Y. S.; Lotsch, B. V; Roling, B.; Vargas-Barbosa, N. M.; Zeier, W. G. How Certain Are the Reported Ionic Conductivities of Thiophosphate-Based Solid Electrolytes? An Interlaboratory Study. *ACS Energy Lett.* **2020**, *5* (3), 910–915. https://doi.org/10.1021/acsenergylett.9b02764.

# For table of contents only



Indium substitution has strong impact on the phase evolution and stacking fault formation in  $\text{Li}_3Y_{1-x}\text{In}_x\text{Cl}_6$ .